NASA-CR-203845

Final Research Report
The University of Alabama in Huntsville

DYNAMICAL MODELS FOR SLOSHING DYNAMICS OF HELIUM II
UNDER LOW-G CONDITIONS

R. J. Hung and Y. T. Long
The University of Alabama in Huntsville
Huntsville, AL 35803

February 1997

Acknowledgement

Abstract

Coupling of sloshing dynamics within a partially filled rotating dewar of superfluid helium II with spacecraft dynamics are investigated in response to the realistic environmental disturbance forces and torques acting on the spacecraft during normal operation. This study investigate: (a) the rotating bubble of superfluid helium II reacting to combined environmental disturbances, including gravity gradient, aerodynamic, and magnetic forces and torques; (b) characteristics of slosh reaction forces and torques coupling with spacecraft dynamics; (c) the contribution of slosh dynamics to over-all spacecraft dynamics; and (d) activating of attitude and translation control system. The numerical computation of sloshing dynamics is based on the rotational frame, while the spacecraft dynamics is associated with non-rotational frame. Results show that the contributions of spacecraft dynamics are driven by the environmental disturbances coupling with slosh dynamics. Without considering the effects of environmental disturbances-driven slosh dynamics acting on spacecraft coupling with the spacecraft dynamics may lead to the wrong results for the development of spacecraft system guidance and attitude control techniques.

I. Introduction

In order to carry out scientific experiments, some experimental spacecraft use cryogenic cooling for observation instrumentation and telescope, superconducting sensors for gyro read-out and maintain very low temperatures near absolute zero for mechanical stability. The approaches to both cooling and control involve the use of helium II. In this study, coupling of spacecraft dynamics with the realistic environmental disturbance forces and torques acting on the spacecraft during normal operation, as well as spacecraft control to maintain the spacecraft normal operation are investigated. The spacecraft adopts the cooling and boil-off from the liquid helium dewar as a cryogen and propellant to maintain the cooling of instruments, attitude and guidance controls and drag-free operation. Potential fluid management problems may arise due to asymmetric distribution of liquid helium and vapor or to perturbations in the liquid-vapor interface. Basic understanding in the coupling of slosh dynamics with six degrees of freedom in spacecraft dynamics plays a significant role in the development of spacecraft guidance and attitude control systems.

Liquid helium II at a temperature of 1.8 K is used as the coolant. With its superfluid behavior, there is very small temperature gradient in the liquid helium. In the negligibly small temperature dependence of surface tension and also the small temperature gradient along the liquid-vapor interface which drive Marangoni convection, the equilibrium shape of the interface is governed by a balance of capillary, centrifugal, gravitational and dynamical forces. Determination of liquid-vapor interface profiles based on computational experiments can uncover details of the flow which can not be easily visualized or measured experimentally in a microgravity environment.

The instability of the liquid-vapor interface can be induced by the presence of longitudinal and lateral accelerations and torques. Thus, slosh waves are excited, producing high and low frequency oscillations in the liquid helium. The sources of the environmental disturbance forces and torques for the operational spacecraft include aerodynamic force and torques, magnetic torques, and gravity gradient forces and torques[1-3]. A recent study[4] suggests that the

high frequency accelerations may be unimportant in comparison with the residual motions caused by low frequency accelerations.

The time-dependent behavior of partially-filled rotating fluids in reduced gravity environments was simulated by numerically solving the Navier-Stokes equations subject to the initial and boundary conditions[5,6]. At the interface between the liquid and the vapor fluids, both the kinematic surface boundary condition and the interface stress conditions for components tangential and normal to the interface were applied[2-3]. The initial conditions were adopted from the steady-state formulations developed by Hung et al[7]. Some of the steady-state formulations of interface shapes were compared with the available experiments carried out by Leslie[8] in a free-falling aircraft (KC-135). The experiments carried out by Mason et al[9] showed that the classical fluid mechanics theory is applicable to cryogenic helium in large containers with sufficiently large velocities[10-13].

At temperatures close to absolute zero, quantum effects begin to be of importance in the properties of fluids. At a temperature of 2.17 K, liquid helium has a λ-point (a second-order phase transition); at temperatures below this point, liquid helium (helium II) has a number of remarkable properties, the most important of which is superfluidity. This is the property of being able to flow without viscosity in narrow capillaries or gaps. At temperatures other than zero, helium II behaves as if it were a mixture of two different liquids. One of these is a superfluid and moves with zero viscosity along a solid surface. The other is a normal viscous fluid. The two motions occur without any transfer of momentum from one to another for velocities below a critical velocity[10-13]. For the components of normal and superfluid velocities above a critical velocity, the two fluids are coupled through snarling in a complex tangle[10-13].

The key parameter of critical velocity to distinguish one-fluid from two-fluid models is a function of fluid temperature and container size. In other words, in considering the dynamical behavior of helium II in a large rotating cylinder, a mixture of the superfluid and the normal fluid without separation of the two fluids for fluid velocities greater than the critical velocity is

2

accounted for in the model computation. Density concentration of superfluid is a function of temperature, which is also true for the surface tension and viscous coefficient for helium II[10-17]. In this study, the theory of viscous Newtonian fluids is employed with transport coefficients being a function of temperature[14,15].

In order to carry out the study of transient phenomena of coupling between slosh reaction torques and spacecraft dynamics, (a) Slosh dynamics based on fluid dynamics formulation, and (b) Spacecraft dynamics and control processes based on translational and rotational formulations, have been numerically solved simultaneously. In the meanwhile, it is true that spacecraft dynamics driven by slosh dynamics can cause the effect to lead spacecraft deviating from normal operation[5]. The results of present study disclose following behavior of spacecraft dynamics: (a) how differences in the dynamical characteristics of environmental disturbances, such as aerodynamic, magnetic and gravity gradient forces and torques contribute to the excitation of slosh waves in liquid-vapor systems, (b) how slosh dynamics provide time-dependent reaction force, torque and mass center fluctuations acting on the spacecraft normal operational systems; and (c) how slosh dynamics contribute to over-all time-dependent force, torque and mass center fluctuations acting on spacecraft during its normal operation under the actuation of attitude and translation control processes.

II. Non-Inertial Frame Mathematical Formulation of Sloshing Dynamics

Experiment made by Andronikashvili[10-13] for rotating helium II shows that it is necessary to exceed a critical velocity for the interaction between the normal and superfluid components to establish entire bucket in rotation[10-13]. For the rotating dewar along outer diameter of 1.56 m and inner diameter of 0.276 m, the critical velocities to assume the interaction between the normal and super-fluid components are 6.4×10^{-7} and 3.6×10^{-6} m/s, respectively[10-15]. With rotating speed of 0.1 rpm, the linear velocities along the outer and inner walls of rotating dewar are 8.17×10^{-3} and 1.45×10^{-3} m/s, respectively, which are at least several hundred times on the order of magnitudes greater than that of the corresponding

critical velocities to assure the interaction between the normal and superfluid components of helium II[10-13]. Based on this illustration, the problem under consideration have the special features to warrant an adoption of viscous Newtonian fluids formulation in this study. These special features are as follows: (a) Fluid velocities are at least several hundred times greater than that of the corresponding critical velocities; (b) These high fluid velocities can produce great enough vortex lines to snarl in a complex tangle to assure an interaction between the normal and superfluid components[10-17]; (c) These vortex lines snarling with a complex tangle between the normal and superfluid components warrant the adoption of Newtonian fluid model[10-17].

Consider a closed circular dewar partially filled with helium II while the ullage is filled with helium vapor. The whole fluid system is spinning in the axial direction z of cylindrical coordinates (r, θ, z), with corresponding velocity components (u, v, w). The governing equations for non-inertial frame spacecraft bound coordinates spinning along its z-axis has been given in our recent studies[20-21]. In this formulation, all the environmental disturbances excluding gravity gradient forces are included in the g-jitter accelerations. In other words, dynamical forces, such as gravity gradient, g-jitter, and angular accelerations, and centrifugal, Coriolis, surface tension, viscous forces, etc., are given explicitly in the mathematical formulations[18-21]. In the computation of sloshing reaction forces, moments, viscous stress and angular momentum acting on the dewar wall of the spacecraft, one must consider those forces and moments in the inertial frame rather than in the non-inertial frame[20-24].

For the purpose of solving sloshing dynamic problems of liquid systems in orbital spacecraft under a microgravity environment, one must solve the governing equations[21,22] accompanied by a set of initial and boundary conditions[23,24]. A detailed illustration of these initial and boundary conditions concerning the sloshing dynamics of fluid systems in microgravity was precisely given in Hung and Pan[20,21,23]. The computational algorithm applicable to cryogenic fluid management under microgravity is also given earlier[21-24]. Summarized computational algorithm are illustrated in Figure 1. In this study, in order to show a

4

realistic example, a dewar with an outer radius of 0.78 m, and an inner radius of 0.138 m, top and bottom radius of 1.10 m and a height of 1.62 m has been used in the numerical simulation. The dewar tank is 80% filled with liquid helium and the ullage is filled with helium vapor (total fluid mass is 287.6 kg). The temperature of liquid helium is 1.8 K. In this study the following data were used: liquid helium density = 145.7 kg/m^3, helium vapor density = 1.47 kg/m^3, fluid pressure = 1.6625 Pa, surface tension coefficient at the interface between liquid helium and helium vapor = 0.0353 N/m, liquid helium viscosity coefficient = 9.61×10^{-9} m^2/s; and contact angle = 0°. The initial profiles of the liquid-vapor interface for the rotating dewar are determined from computations based on algorithms developed for the steady state formulation of microgravity fluid management[7,23-25].

A staggered grid for the velocity components is used in this computer program. MAC (marker-and-cell) method[26] of studying fluid flows along a free surface is adopted. VOF (volume of fluid) method is used to track the dynamic behavior of liquid-vapor interface by solving finite difference equations numerically. Detailed computational algorithm are illustrated in Figure 1. The approximate flow velocity is calculated from the explicit approximation of momentum equations based on the results from the previous time step. Computation of pressure and velocity at the new time step are, thus, obtained from iteratively solving the pressure equation through conjugate residual technique[27-30]. The configuration of liquid-vapor interface adjusted by the surface tension effect at the new time step are then finally obtained. The time step during this computation is automatically adjusted through the fulfillment of the stability criteria of computed grid size. Convergence criterion of the iteration of pressure equation is based on the computed velocity at each cell which satisfy continuity equation with the errors no more than 10^{-5} of the velocity difference[31]. As for the volume conservation of liquid, a deviation of less than 1 % error of volume is always guaranteed before a move to the next time step.

5

III. Characteristics of Environmental Disturbance Forces and Torques Acting on the Fluid Systems and Spacecraft

To give an example of the GP-B Spacecraft, which is an Earth satellite orbiting at 650 km altitude directly over the poles, the orbit period, τ_o can be computed from following expression:

$$\tau_o = 2\pi \frac{R_c^{3/2}}{R_E g_o^{1/2}} \qquad (s) \qquad (3-1)$$

where R_E denotes the radius of Earth (= 6373 km); R_o, the radius of the circular orbit (= R_E + h = 7023 km); h, orbit altitude (= 650 km); and g_o, Earth gravity acceleration (= 9.81 m/s^2). For the case of GP-B, the orbit period τ_o = 97.6 min (5856 s), and orbit rate n = $2\pi/\tau_o$ = 1.07 x 10^{-3} rad/s.

(A)   Gravity Gradient Forces and Torques

The gravity gradient acceleration acting on the fluid mass of spacecraft can be shown as[18-21]

$$\hat{a}_{gg} = -n^2 [3(\hat{r}_c \cdot \hat{d})\hat{r}_c - \hat{d}] \qquad (m/s^2) \qquad (3-2)$$

where $\hat{a}_{gg}$ denotes gravity gradient acceleration vector; $\hat{d}$, the vector (not an unit vector) from the fluid element to the spacecraft mass center; $\hat{r}_c$, an unit vector from the spacecraft mass center to the center of the Earth; and n, the orbit rate.

To give an example of the GP-B Spacecraft, it is assumed that the gravity gradient exerted on the mass center of the spacecraft orbiting around the Earth on its specified orbit is zero. In other words, all the gravity acceleration exerted on the spacecraft is nothing but the gravity gradient acceleration which is defined in Equation (3-2). In this study, we are interested in investigating how gravity gradient acceleration affects the dynamical behavior of cryogenic fluid elements of helium and excite capillary effect governed liquid-vapor-solid interface disturbances.

For the convenience of mathematical calculation, let us describe all the parameters involved in Equation (3-2) in terms of Cartesian coordinates. In

6

order to match with the computer simulation, mathematical derivation are considered in the first quadrant. Figure 2(A) illustrates the geometrical relationship of the parameters shown in Equation (3-2).

For the case of GP-B, spacecraft is rolling about its boresight axis in a polar, 650 km altitude Earth orbit with the spacecraft boresight pointing at Rigel. The vehicle is rolling at a constant angular velocity about its boresight axis, while the boresight remains inertially fixed on Rigel. At time t = 0, the rolling axis of the spacecraft is aligned with the radial direction of the Earth center to the spacecraft mass center. Azimuth angle of Earth toward the location of the spacecraft mass center, ψ_s, can be computed from the orbit period obtained from Eq.(3-1) under the normal operation of spacecraft

$$\psi_E = 2\frac{\pi}{\tau_o}t \tag{3-3}$$

where t is the time measured from the instant when the direction of spacecraft spinning axis is aligned with the radial direction of spacecraft mass center to the center of the Earth. Some modification is required if coupling of slosh and orbital dynamics in which the results of the spacecraft orbit deviating from normal operation are considered.

Gravity gradient acceleration indicates that acceleration acting on any fluid mass inside the container increases two units of acceleration per unit of distance measured from the mass center of the container (point O_g at Figure 2A) to the location of the fluid mass parallel along the radial axis from the mass center of the container to the center of the Earth (parallel to unit vector $\hat{r}_c$ shown in Figure 2A) while the acceleration acting on the fluid mass decreases one unit of acceleration per unit of the shortest distance measured from the location of the fluid mass to the radial axis along the vector from the mass center of the container to the center of the Earth[18-20].

On the other hand, gravity gradient torque $\hat{M}_g$ in the non-inertial frame of spacecraft bound coordinates is given by

$$\hat{M}_g = \int (\hat{a}_{gg} \times \hat{d}) \, dm = 3n^2 [\, \hat{r}_c \times (\hat{I} \cdot \hat{r}_c)\,] \qquad (N \cdot m) \tag{3-4}$$

where m (kg) denotes mass of the spacecraft dry mass, while $\hat{I}$ is the inertia tensor (kg.m²) in the non-inertial frame. For the case of GP-B with a mass of 3000 kg, the dry mass inertia tensor in the body coordinate frame[32] is

$$\hat{I} = \begin{bmatrix} 4777 & 0 & 0 \\ 0 & 4777 & 0 \\ 0 & 0 & 3489 \end{bmatrix} \quad (kg \cdot m^2) \tag{3-5}$$

Figure 3(A) shows the time variation of gravity gradient torque acting on the spacecraft systems for a full orbit period with component along (x,y,z) directions. It shows a harmonic oscillation in x- and y-directions in which peaks of the oscillations coincide with the quarter orbit periods of spacecraft. Gravity gradient torque acting on the spacecraft system along z-direction is relatively small and is on the 10^{-2} order of magnitude smaller in comparison with that of the components in x- and y-directions.

(B)   Aerodynamic Forces and Torques

Aerodynamic forces and torques are caused by molecular collisions of Earth atmospheric gases on exterior spacecraft surfaces, resulting in momentum and energy transfer. For the case of GP-B orbiting at 650 km above Earth in a circular, polar orbit with velocity vector magnitude v, the spacecraft encounters atmospheric gas with fluctuating density ρ. For a constant reference area A_r and length L_r, the aerodynamic forces and torques in the spacecraft bound frame are computed from

$$F_{ai} = \frac{1}{2} \rho v^2 A_r C_{fi} \tag{3-6}$$

$$M_{ai} = \frac{1}{2} \rho v^2 A_r L_r C_{mi} \tag{3-7}$$

where non-dimensional force C_{fi} and torque C_{mi} coefficient vectors along direction i in the spacecraft bound frame represent the influence of spacecraft shape,

including aerodynamic shading effects, on the aerodynamic forces and torques, respectively. The force and torque coefficients are computed for all vehicle pitch and roll angles of the body frame. At 650 km altitude of free molecular flow region (mean free path = 2 X 10^5 m), the momentum transfer is characterized entirely as interaction between incident gas molecules upon spacecraft surfaces which is a function of incident flow angle, molecular speed ratio, temperature, and surface roughness. The shading algorithm used in computing the aerodynamic force and torque coefficients sums elemental forces and torques only for those elements directly exposed to the incoming free molecular flow. Figures 2(C) and 3(B) show time variation of aerodynamic forces and torques, respectively, along (x,y,z) directions with reference to Lockheed User's Handbook[32] extending in a full orbit period. It shows a series of harmonic oscillations with greater amplitudes of oscillations in terms of azimuth angle ψ_z in the ranges of $-\pi/4 <$ $\psi_z < \pi/4$, and $3\pi/4 < \psi_z < 5\pi/4$ whereas smaller amplitudes of oscillations occur in the ranges of $\pi/4 < \psi_z < 3\pi/4$, and $5\pi/4 < \psi_z < 7\pi/4$ for components along x- and y-directions. These results illustrate a fact that the spacecraft encounters a maximum drag when the incoming flow is along lateral or transverse direction of the spacecraft while the drag becomes minimum when the incoming flow is along the axial or longitudinal direction of the spacecraft for drag force and torque components along x-, and y-directions. As to the components of aerodynamic forces and torques along z-direction, it show a half cycle oscillation with respect to orbital period in which a negative value is resulted for the first half cycle (spacecraft translation along -z direction) whereas a positive value is shown for the second half cycle (spacecraft translation along +z direction) of the orbital period.

(C)   Magnetic Torques

Magnetic torques on the spacecraft are due to interaction between the cryoperm shield and Earth magnetic field through the production of cryoperm magnetic dipole induced by the Earth magnetic field. Demagnetization coefficients characterize the vector relationship between the exterior magnetic field and the induced dipole for the shield. Although the cryoperm shield is

9

axially symmetric about the spacecraft boresight, unequal transverse axis demagnetization coefficients were used to construct the cryoperm shield dipole. An external magnetic torque $\hat{M}_m$ (N·m) occurs when the GP-B cryoperm shield magnetic dipole vector $\hat{D}_m$ (A·m²) is in the presence of the Earth magnetic field B (Tesla), namely,

$$\hat{M}_m = \hat{D}_m \times \hat{B} \qquad (N \cdot m) \qquad (3-8)$$

All vectors are in body frame coordinates. Figure 3(C) shows time variation of magnetic torques along (x,y,z) directions with referenced to Lockheed User's Handbook[32] extending in a full orbit period. It shows a series of harmonic oscillations while spacecraft completes a loop of orbit period along polar orbit across dipole geomagnetic fields of Earth along x- and y-directions. Magnetic torque acting on the spacecraft system along z-direction is relatively small and is on the order of 10^{-2} order of magnitude smaller in comparison with that of the components in x- and y-directions.

Characteristics of gravity gradient, aerodynamic and magnetic forces and torques acting on fluids and spacecraft systems are quite different. As to the dynamics of fluid systems, both gravity gradient and aerodynamic forces can activate fluid elements directly with the help of fluid dynamic equations, whereas the activation of gravity gradient, aerodynamic and magnetic torques on fluid elements have to be computed indirectly in fluid dynamic equations from angular velocities and angular accelerations which are coupled directly with spacecraft rotational equations. It is also interesting to note for differences between forces of direct contact, and forces of contact with distances (such as gravitational and magnetic forces). In the present case of helium II fluids in rotating dewar, aerodynamic forces belong to forces of direct contact whereas gravity gradient forces are forces of contact with distances. There is no magnetic force acting on the helium II fluids directly because there is an interaction between cryoperm shield and geomagnetic fluid but not directly with helium II fluids. Comparison between the characteristics of gravity gradient and aerodynamic forces acting on the fluid masses show that gravity gradient forces

10

activate different magnitudes of forces on the fluid masses at different locations inside the dewar whereas aerodynamic forces drive same magnitude on fluid masses everywhere inside the dewar via forces of reaction through the container wall.

IV Attitude and Translation Control Subsystem

The following description of the GP-B Attitude and Translation Control Subsystem is a simplified version of LMSC/P08701, <u>GP-B Attitude and Translation Control Subsystem Description</u>[33], provided by Lockheed in support of the GP-B design.

(A) Attitude Control

The attitude control system is based on a proven design used on the Hubble Space Telscope. The attitude control function generates the spacecraft torque command which is sent to the helium thruster control function. The nominal configuration uses a Proportional/Integral (PI) type control law with rate feedback and a roll rate filter which adds gain in the forward loop to attenuate disturbances at the roll frequency. Rate feedback is accomplished by using low-noise rate-integrating gyros and limiters are used to allow rate limited capture and maneuvers.

(a) Inputs:

ω_{err} – Vehicle rate error (rad/s)

θ_{err} – Vehicle attitude error (rad)

(b) Parameters:

Control Gains

	Pitch/Yaw	Roll	
Proportional Gain:	$K_p = 0.482$	$K_p = 0.054$	(s^{-2})
Rate Gain:	$K_r = 1.98$	$K_r = 7.26$	(s)
Integral Gain:	$K_i = 0.25$	$K_i = 0.0023$	(s^{-1})

Pitch/Yaw loop bandwidth = 0.15 cycles/s

Roll loop bandwidth = 0.06 cycles/s

11

Constants are used to limit the value of some of the variables in the control processing logic. Limits of these constants are as follows:

Pitch/Yaw (bw = 0.15 Hz)		Roll (bw = 0.06 Hz)	
Lm1 = 1	arcsec	Lim1 = 60	arcsec
Lm2 = 0.01	arcsec	Lim2 = 0.05	arcsec
Lm3 = 1	arcsec	Lim3 = 60	arcsec
Lm4 = 0.25	arcsec	Lim4 = 20	arcsec
Lm5 = 0.05	arcsec	Lim5 = 4	arcsec
Lm6 = 0.25	arcsec	Lim6 = 20	arcsec
Lm7 = 0.25	arcsec	Lim7 = 20	arcsec

(c) Outputs

Tcmd = Vehicle Torque Command

(d) Processing:

Calculations are applied to each axis (pitch, yaw, roll) every 0.1 s. The output is a vehicle torque command the designated axis updated at the 10 Hz rate. In this calculation, x(n) refers to the value of x at the current control sample; and x(n-1) refers to the value of x at the previous control sample (delayed 0.1 s). Processing of calculations are as flows:

1. Apply limit function to attitude error

θ_{err_l} - Attitude Error limited

$\theta_{err\_l} = Lim1(\theta_{err})$

where Limit Function (Saturation) is:

Lim1(i) = i, if -Lim1 < i < Lim1

Lim1(i) = Lim1, if i > Lim1; and

Lim1(i) = -Lim1, if i < -Lim1

2. Compute integral path for attitude control

$\theta_{Int}(n) = Lim5[\theta_{Int}(n-1)] + K_i \theta_{err\_l}(n-1)$ dt

where $\theta_{Int}(n)$ - Integral path - attitude error for current time step; and dt = 0.1 s - control loop sample time

3. Apply Roll Rate Filter to Attitude Control

(i) $u_r(n)$ - Roll filter input at the current time step

$$u_r(n) = \theta_{Int}(n) + Lim4[\theta_{err}(n)] + Lim6[K_r \, \omega_{err}(n)]$$

(ii) $x_r(n)$ - Roll filter state at the current time step

$$x_r(n) = A_r \, x_r(n-1) + B_r \, u_r(n)$$

(iii) $y_r(n)$ - Roll filter output at the current time step

$$y_r(n) = C_r \, x_r(n-1) + D_r \, u_r(n)$$

(iv) A_r - Roll filter state transition matrix

$$A_r = \begin{bmatrix} -d_1 & -d_2 \\ 1 & 0 \end{bmatrix}$$

where filter coefficients: $d_1 = -1.9999926$, and $d_2 = 0.9999937$

(v) B_r - Roll filter input matrix

$$B_r = \begin{bmatrix} 1 \\ 0 \end{bmatrix}$$

(vi) C_r - Roll filter output matrix

$$C_r = [(n_1 - n_0 d_1), \ (n_2 - n_0 d_2)]$$

where filter coefficients: $n_0 = 1.0031384$, $n_1 = -1.9999926$, and $n_2 = 0.9968553$

(vii) Dr - Rollfilter input / output coupling matrix

$$B_r = [n_0]$$

4. Compte Torque Command

$$T_{cmd}(n) = K_p \cdot I \cdot Lim7 [y_r(n)]$$

where I - Vehicle Inertia about designated axis; and

T_{cmd} - Vehicle Torque Command for designated axis

(B) Translational Dynamics

The translational motion of proof mass with respect to the spacecraft (i.e. proof mass housing) is sensed by the capacitive pick-off sensor (drag-free

13

sensor) and used by the translational control function to control the spaceceaft translation. This is done to reduce inertial accelerations of the proof mass. The method demonstrates the method for determining the proof mass position error (i.e. - location of the proof mass housing with respect to the proof mass). Steps of these methods are as folows:

1. Sum all forces on the dry spacecraft (i.e. aerodynamics, magnetics, Helium slosh, ...).

2. Convert the total forces to inertial coordinates and solve translational equations of motion for the location of the dry spacecraft center of mass. The proof mass is assumed to be free from inertial forces and is located at the origin of the inertial coordinate frame.

3. Compute the location of the proof mass housing relative to the proof mass by converting the center of mass to vehicle coordinates and adding the location of the proof mass housing relative to the spacecraft center of mass.

    $$R_{pmh\_pm} = R_{pmh\_cm} + R_{cm\_pm}$$

    where R_{pmh_pm} - location of the proof mass housing relative to the proof mass; R_{pmh_cm} - location of the proof mass housing relative to the center of mass; and R_{cm_pm} - location of the center of mass housing relative to the proof mass.

(C) Trsanslational Control

The translational control function generates the spacecraft force commands sent to the Helium thrusters. The normal configuration uses Proportional/Integral/Derivative (PID) type control law and a roll rate filter which adds gain in the forward loop to attenuate disturbances at the roll freqency. Positon feedback is accomplished by monitoring the proof mass positon with respect to t he spacecraft (proof mass housing) using a capacitive pick-off sensor.

(a) Inputs:

R_{pmh_pm} - location of the proof mass housing relative to the proof mass(m)

(b) Parameters:

14

(i)   Control Gains

Each Axis (bw = 0.5 Hz)

Proportional gain K_p = 2.44

Rate gain k_r = 1.2345

Integral gain K_i = 0.605

(ii)   Constants used to limit the value of some of the variables in the control processing logic.

The limits are as follows:

Each Axis (bw = 0.5 Hz)

Lim1 = 5×10^{-7} m

Lim2 = 0.005 N

(c) Outputs

F_{cmd} – Vehicle Force Command

(d) Processing:

Calculations are applied to each axis every 0.1 s. The output is a vehicle force command for the designated axis updated at the 10Hz. rate.

In this calculation:

X(n) refers to the value of X at the current control sample; and

X(n-1) refers to the value of X at the previous control sample(delayed 0.1 s).

Processing of calculations are as follows:

1. Compute the proof mass error

R_{err} – Proof mass position error

R_{err} = $-R_{pmh\_pm}$

2. Compute integral path for translational control

$R_{Int}(n)$ = Lim1[$R_{Int}(n-1)$] + $K_i R_{err}(n-1)dt$

where $R_{Int}(n)$ – Interal path – proof mass error for current time step;

and dt = 0.1 sec – control loop sample time

3. Apply Roll Rate Filter to Translational Control

(i) $u_r(n)$ – Roll filter input at the current time step

$u_r(n)$ = $R_{Int}(n)$ + $R_{err}(n)$ + $K_r [R_{err}(n) - R_{err}(n-1)]/dt$

(ii) $x_r(n)$ - Roll filter state at the current time step

$$x_r(n) = A_r x_r(n-1) + B_r u_r(n)$$

(iii) $y_r(n)$ - Roll filter output at the current time step

$$y_r(n) = C_r x_r(n-1) + D_r u_r(n)$$

(iv) A_r - Roll filter state transiton matrix

$$A_r = \begin{bmatrix} -d_1 & -d_2 \\ 1 & 0 \end{bmatrix}$$

where filter coefficients: $d_1 = -1.9999926$, and $d_2 = 0.9999937$

(v) B_r - Roll filter input matrix

$$B_r = \begin{bmatrix} 1 \\ 0 \end{bmatrix}$$

(vi) C_r - Roll filter output matrix

$$C_r = [(n_1 - n_0 d_1), \ (n_2 - n_0 d_2)]$$

where filter coefficients: $n_0 = 1.0031384$, $n_1 = -1.9999926$, and
$n_2 = 0.9968553$

(vii) Dr - Rollfilter input / output coupling matrix

$$B_r = [n_0]$$

4. Compute force Command

$$F_{cmd}(n) = Lim2[K_p \cdot m \cdot y_r(n)]$$

where m - Vehicle dry mass; and F_{cmd} - Vehicle Force Command for
designated axis

V Mathematical Formulation of Spacecraft Dynamics

In spacecraft dynamics, a rigid body with six degrees of freedom, three
being translational and three rotational, is considered. In this study, our

primary interest is to investigate the dynamical behavior of spacecraft driven by the coupling between each individual gravity gradient, aerodynamics, magnetic forces and torques, and the combined effects of these forces and torques coupling with spacecraft dynamics.

The governing equations of three translational equations are given by

$$\frac{d}{dt}(m\dot{X}_i) = F_{Di} + F_{Li} + F_{Ci} \tag{5-1}$$

where m, X, F_D, F_c and F_L denote mass of spacecraft, inertial frame (non-rotational) coordinate, environmental forces such as gravity gradient and/or aerodynamic forces acting on the spacecraft, control force and slosh reaction forces (feedback from fluid system) acting on the spacecraft, respectively. Subscript i denotes component along direction i (=X,Y, or Z in non-rotational frame), while single dot and double dots at top $(\dot{X}, \ddot{X})$ imply first and second order time derivatives of the parameter, respectively. Eulerian angles are defined to accommodate three rotational equations[34]. As usual, ψ, θ, and ϕ are defined as the heading, attitude and bank angles[34]. Three rotational equations in terms of Eulerian angles are given by

$$I_t(\ddot{\theta}+\dot{\psi}^2\sin\theta\cos\theta)+I_a\dot{\psi}\cos\theta(\dot{\phi}-\dot{\psi}\sin\theta) = M_\theta \tag{5-2}$$

$$I_a[(-\ddot{\phi}+\dot{\psi}\sin\theta+\dot{\psi}\dot{\theta}\cos\theta)\sin\theta-\dot{\theta}(\dot{\phi}-\dot{\psi}\sin\theta)\cos\theta] \\ +I_t(\ddot{\psi}\cos^2\theta-2\dot{\psi}\dot{\theta}\sin\theta\cos\theta) = M_\psi \tag{5-3}$$

$$I_a(\ddot{\phi}-\ddot{\psi}\sin\theta-\dot{\psi}\dot{\theta}\cos\theta) = M_\phi \tag{5-4}$$

Where

$$M_\theta = (M_{Lx}+M_{Dx}+M_{Cx})\cos\phi-(M_{Ly}+M_{Dy}+M_{Cy})\sin\phi \tag{5-5}$$

$$M_\psi = (M_{Lx}+M_{Dx}+M_{Cx})\sin\phi\cos\theta+(M_{Ly}+M_{Dy}+M_{Cy})\cos\phi\cos\theta \\ -(M_{Lz}+M_{Dz}+M_{Cz})\sin\theta \tag{5-6}$$

17

$$M_\phi = (M_{Lz} + M_{Dz} + M_{Cz}) \qquad\qquad (5-7)$$

where M_{Li}, M_{Di} and M_{Ci} are slosh reaction torque acting on the dewar and environmental disturbance torques (such as gravity gradient, aerodynamic and/or magnetic torques) and control torque acting on spacecraft, respectively, along direction i. M_{Li}, M_{Di} and M_{Ci} are defined in non-inertial (rotational) frame. With reference to Equation (3-5) for GP-B moments of inertia, $I_1 = I_{xx}$, $I_2 = I_{yy}$ and $I_3 = I_{zz}$. I_a ($= I_3$) and I_t ($= I_1 = I_2$) denote moment of inertial along axial and transverse directions, respectively.

Activation of slosh dynamics in response to environmental disturbance forces and torques coupling with spacecraft dynamics certainly will induce angular velocity ($\omega_1, \omega_2, \omega_3$) along (x,y,z) coordinates in rotational frame. Let $(\omega_1, \omega_2, \omega_3) = (\dot\theta_1, \dot\theta_2, \dot\theta_3 + \omega)$, $(\dot\theta_1, \dot\theta_2, \dot\theta_3)$ are the time derivative of angular displacement along (x,y,z) coordinates, and ω denotes dewar rotating speed along z-axis. With the assumption of axially symmetric body about the z-axis, Eulerian equations shown in Equations (5-2) to (5-4) can be rewritten and expressed as[12]

$$\ddot\theta_1 + K_1 \dot\theta_2 (\dot\theta_3 + \omega) = \frac{1}{I_1} (M_{Lx} + M_{Dx} + M_{Cx})$$

$$\ddot\theta_2 + K_2 \dot\theta_1 (\dot\theta_3 + \omega) = \frac{1}{I_2} (M_{Ly} + M_{Dy} + M_{Cy}) \qquad\qquad (5-8)$$

$$\ddot\theta_3 + K_3 \dot\theta_1 \dot\theta_2 = \frac{1}{I_3} (M_{Lz} + M_{Dz} + M_{Cz})$$

in rotational frame, where $K_1 = (I_3 - I_2)/I_1$, $K_2 = (I_1 - I_3)/I_2$, and $K_3 = (I_2 - I_1)/I_3$.

Both translational and rotational equations are initial-valued problems. Initial conditions for the translational equations are

$$\left.\begin{array}{l} (X,Y,Z) = (0,0,0)\ cm,\ and \\[2mm] (\dot X, \dot Y, \dot Z) = (0,0,0)\ cm/s \quad at\ t = 0 \end{array}\right\} \qquad\qquad (5-9)$$

and that for the rotational equations are

$$(\theta, \psi, \phi) = (0, 0, 0) \; rad, \; and$$

$$(\dot{\theta}, \dot{\psi}, \dot{\phi}) = (0, 0, 0.1) \; rpm \quad at \; t = 0 \qquad \biggr\} \qquad (5\text{-}10)$$

In this paper, rotational frame is adopted in the study of sloshing dynamics while non-rotational frame is chosen in the investigation of spacecraft dynamics. Conversion matrix A shall be used to make the conversion from the parameters in non-rotational frame (X,Y,Z) to that of the parameters in rotational frame (x,y,z) through the execution of following mathematical expression:

$$\begin{bmatrix} x \\ y \\ z \end{bmatrix} = A \begin{bmatrix} X \\ Y \\ Z \end{bmatrix} \qquad (5\text{-}11)$$

where

$$A = \begin{bmatrix} A_{XX} & A_{XY} & A_{XZ} \\ A_{YX} & A_{YY} & A_{YZ} \\ A_{ZX} & A_{ZY} & A_{ZZ} \end{bmatrix} \qquad (5\text{-}12)$$

$A_{XX} = -\sin\psi\cos\phi + \cos\psi\sin\theta\sin\phi$, $A_{YX} = \sin\psi\sin\phi + \cos\psi\sin\theta\cos\phi$, $A_{ZX} = \cos\psi\cos\theta$,

$A_{XY} = \cos\psi\cos\phi + \sin\psi\sin\theta\sin\phi$, $A_{YY} = -\cos\psi\sin\phi + \sin\psi\sin\theta\cos\phi$, $A_{ZY} = \sin\psi\cos\theta$,

$A_{XZ} = \cos\theta\sin\phi$, $A_{YZ} = \cos\theta\cos\phi$, and $A_{ZZ} = -\sin\theta$.

As A is an orthogonal matrix, $A^{-1} = A^{T}$, Equation (5-11) becomes

$$\begin{bmatrix} X \\ Y \\ Z \end{bmatrix} = A^{T} \begin{bmatrix} x \\ y \\ z \end{bmatrix} \qquad (5\text{-}13)$$

Equations (5-11 to (5-15) shall be solved simtaneously to determine the values of the parameters of interest. Detailed algorithm of solving these equations coupling with slosh dynamics of fluid equation are illustrated in Figure 4.

VI Slosh Dynamics of Spacecraft

Slosh dynamics driven by environmental forces and torques coupling with

spacecraft dynamics can be computed from Sections II, III, IV and V simultaneously. Figure 5(A) shows grid generation in which three-dimensional dewar, r-z plane at $\theta = 0°$, and r-θ plane at z = L/2 are illustrated in Figures 5(A-a), 5(A-b) and 5(A-c), respectively, where L is the height of dewar. Figure 5(B) shows initial profiles of liquid-vapor interface with liquid fill level of 80% in which three-dimensional, r-z plane at $\theta = 0°$, and r-θ plane at z = 108 cm are illustrated in Figures 5(B-a), 5(B-b) and 5(B-c), respectively. Here, initial interface profiles are computed under the conditions of g = 10^{-7} g_o, ω = 0.1 rpm and $\psi_x = 0°$. Characteristics of slosh dynamics driven by each individual and combined environmental disturbance forces and torques coupling with spacecraft dynamics are investigated.

Combined environmental disturbances, including gravity gradient, aerodynamic, and magnetic and control forces and torques, acting on fluid systems of dewar coupling with spacecraft dynamics are considered[35, 36]. Figure 6 shows the time sequence evolution of the three dimensional dynamical behavior of liquid-vapor interface oscillations driven by these combined environmental disturbances. It shows a series of asymmetric oscillations excited along liquid-vapor interface driven by these combine environmental disturbances.

Figure 7 shows sloshing affected time evolution of fluid mass center fluctuations (in rotational frame) driven by combined environmental disturbances coupling with spacecraft dynamics. The values of fluid mass center fluctuations and their maximum absolute values are Max (Δx_{Lc}, Δy_{Lc}, Δz_{Lc}) = (1.47, 0.84, 5.6) mm, and Max ($|x_{Lc}|$, $|y_{Lc}|$, $|z_{Lc}|$) = (0.87, 0.44, 3.3) mm. These results imply Δz_{Lc} > Δx_{Lc} > Δy_{Lc}, and $|z_{Lc}|$ > $|x_{Lc}|$ > $|y_{Lc}|$.

Over-all slosh reaction forces and torques driven by combined environmental forces and torques have been investigated. Figure 8(A) shows the computed time variation of the fluctuations of slosh reaction forces (in rotational frame) exerted on the dewar in response to the combined environmental forces, and torques coupling with spacecraft dynamics. This figure shows the following results: (a) The values of slosh reaction force fluctuations and their maximum absolute values are Max (ΔF_{Lx}, ΔF_{Ly}, ΔF_{Lz}) = (3.6, 2.6, 5.7) 10^{-4} N, and Max ($|F_{Lx}|$,

$|F_{Ly}|$, $|F_{Lz}|$) = (2.0, 1.5, 2.9) 10^{-4} N, respectively, which imply $\Delta F_{Lz} > \Delta F_{Lx} > \Delta F_{Ly}$, and $|F_{Lz}| > |F_{Lx}| > |F_{Ly}|$. (b) Comparison of the characteristics of fluid mass center fluctuations and slosh reaction forces driven by combined environmental disturbances show that amplitude and fluctuations along the axial direction are greater than that along transverse directions. (c) Figures 9(A-a), 9(A-b), and 9(A-c) show power spectral density with peak values of frequencies for autospectral analysis of slosh reaction forces exerted on the dewar in response to combined environmental disturbances along x, y and z directions, respectively. Major peaks shown are similar to the results concluded earlier.

Figure 8(B) shows time variations of slosh reaction torques (in rotating frame) exerted on the dewar in response to the combined environmental forces and torques coupling with spacecraft dynamics. The values of slosh reaction torque fluctuations and their maximum absolute values are Max (ΔM_{Lx}, ΔM_{Ly}, ΔM_{Lz}) = (1.6, 1.7, 10^{-3}) 10^{-4} N·m, and Max ($|M_{Lx}|$, $|M_{Ly}|$, $|M_{Lx}|$) = (0.8, 0.7, 0.6x10^{-3}) 10^{-4} N·m, respectively. This figure shows the following results: (a) $\Delta M_{Lx} \sim \Delta M_{Ly} \gg \Delta M_{Lz}$, and $|M_{Lx}| \sim |M_{Ly}| \gg |M_{Lz}|$. This means that the major slosh reaction torques driven by fluid systems exerted on the dewar in rotational frame are in the transverse rather than in the longitudinal directions. (b) Figures 9(B-a), 9(B-b) and 9(B-c) show power spectral density with peak values of frequencies for autospectral analysis of slosh reaction torques exerted on the dewar in response to the combined environmental forces and torques along x, y, and z directions, respectively. Major peaks shown are similar to the results concluded earlier.

VII Control Force and Torque

Figure 10(A) and 10(B) show the components of control forces and torques, respectively, along X, Y and Z direction based on the formulations of control equations illustrated in Section IV.

Comparison between Figures 2(B) and 10(A) shows both characteristics of force variations and amplitude fluctuations for control forces and aerodynamics forces are basically similar except that there is out-of-phase for 180°. In other words, these two forces are equal in magnitude and opposite in direction. This also explains that major forces which drive spacecraft deviating from normal orbit are contributed by aerodynamic forces. In the meanwhile, fluid sloshing forces acting on the spacecraft also drive spacecraft deviating from normal

operation. Components of high frequency fluctuations imposed on the time-dependent variations of control forces are the results of product contributed by fluid sloshing forces acting on the spacecraft .

Computed absolute values of maximum amplitudes for control forces are $(|F_{cx}|, |F_{cy}|, |F_{cz}|) = (2.6, 3.6, 2.5) \ 10^{-3}$ N, while the saturation value (Lim2) of control subsystem documentation projects are 5×10^{-3} N. In other words, the amplitudes of control forces are not exceeding the saturation value during the processes of normal spacecraft operation based on this computation.

Main environmental torques acting on the spacecraft are contributed by gravity-gradient, magnetic and aerodynamic torques. Based on the order of disturbances, these torques are on the order of 10^{-3} N·m. On the other hands, Figure 8(B) shows that the order of magnitude for slosh reaction torque is on the order of 10^{-3} N·m. This explains that the major deviation of spacecraft control shall be concentrated on the correction of combined effect resulting from spacecraft torque disturbances due to angular deviation from normal operation.

VIII Resultant Forces and Resultant Torques

Based on definition, total forces and torques acting in the spacecraft are $F_i = F_{Li} + F_{Di} + F_{ci}$, and $M_i = M_{Li} + M_{Di} + M_{ci}$, respectively. Computed total forces and torques are illustrated in Figure 11(A) and 11(B). For the convenience of comparison, both F_i and M_i are transferred to rotational coordinates.

Figure 11(A) shows that the order of magnitude for the total resultant forces are on the order of 10^{-4} N and are fluctuating from positive to negative values around the surrounding of 0 value when t>200 s. Computed results indicate that the absolute values of maximum amplitude of total resultant forces are $(|F_x|, |F_y|, |F_z|) = (5.97, 4.23, 22.35)10^{-3}$ N. The range of maximum fluctuation of total resultant forces are $(\Delta F_x, \Delta F_y, \Delta F_z) = (9.15, 6.35, 4.30)10^{-3}$ N. The main cause of these maximum value fluctuations are induced by the fluid sloshing forces-related fluctuations at the beginning of computer simulation. In this computation, it is assumed that liquid helium is in static condition inside the rotating dewar in rotational frame at t = 0. Fluid is subjected to various environment forces which drive the fluid to non-equilibrium status in addition to the nature of incompressibility that make the initiation of large amplitude slosh oscillations which are fedback to spacecraft at t>0. Fluid slosh damp out

gradually, and become the status of normal fluctuations after t>200 s.

Similarly, characteristics of total resultant torques demonstrate the similar manner as that of total resultant forces illustrated earlier. The order of magnitude of total resultant torques are on the order of 10^{-4} N·m. The absolute value of the maximum resultant torque are ($|M_x|$, $|M_y|$, $|M_z|$) = (2.62, 1.86, 1.18)10^{-3} N·m. The range of maximum fluctuations of total resultant torque are (ΔM_x, ΔM_y, ΔM_z) = (4.58, 3.45, 2.29)10^{-3} N·m.

IX Attitude Errors

Figures 12(A) and 12(B) show spacecraft angular rate errors and attitude errors, respectively. In the spacecraft normal operation, characteristics of angular velocity variation in rotating frame is (ω_x, ω_y, ω_z) = (0, 0, 0.1) rpm. To illustrate the errors of angular velocity, Figure 12(A) shows the value of spacecraft angular velocity errors in terms of $\Delta\omega_z = \omega_z - \omega_{z0}$, where ω_z denotes the actual value of the component of spacecraft angular velocity along z-axis while ω_{z0} shows angular velocity of spacecraft at normal operation (i.e., ω_{z0} = 0.1 rpm).

Absolute values of maximum angular velocity deviating from normal operation are ($|\omega_x|$, $|\omega_y|$, $|\Delta\omega_z|$) = (9.8, 22.1, 2.8)10^{-8} rad/s. The range of maximum fluctuations of angular velocity deviating from normal operation are ($\Delta\omega_x$, $\Delta\omega_y$, $\Delta(\Delta\omega_z)$) = (15.4, 38.4, 6.25)10^{-8} rad/s. In fact, these maximum values of fluctuations occur at the initial stage of the simulation. As indicated earlier, fluid inside the rotating dewar starts to receive environmental disturbances suddenly at t>0, this sudden induction of environmental disturbances introduce large amplitude fluctuations on the slosh dynamics and spacecraft system. Figure 12(B) shows the value of spacecraft rotating angle errors in terms of $\Delta\phi = \phi - \omega_{z0}t$, where ω_{z0} denotes time variation of spacecraft normal operation with rotating angle ϕ, and t is time. In this expression, ϕ is actual value of angular displacement. During the spacecraft normal operation, $\psi = \theta = 0$. Figure 12(B) also illustrates the time dependent variations of parameters ψ, θ and $\Delta\phi$ deviating from normal operation. The absolute values of maximum attitude errors are ($|\psi|$, $|\theta|$, $|\Delta\phi|$) = (5.4, 114.8, 0.6)10^{-7} rad, while the range of maximum fluctuations of attitude errors are ($\Delta\psi$, $\Delta\theta$, $\Delta(\Delta\phi)$) = (7.14, 30, 11.18)10^{-7} rad.

In this computation, sensor sensitivity to measure angular rate errors and

attitude errors are not included in our model. In fact, it is assumed that the corresponding control forces and torques will activate the spacecraft control systems based on control functions so long as there are angle errors and attitude errors no matter how small the amplitudes they are. This explains the magnitude of angle rate errors and attitude errors are so small. Similar results are also obtained for translational errors. The magnitudes of these errors will be amplified if sensor sensitivity and/or measurement errors are estimated and are taken into consideration.

X Translational Errors

Figures 13(A), 13(B) and 13(C) show translational acceleration, velocity and displacement errors, respectively, in non-rotating frame, with the activation of control system under normal operation. These figures show that the range of fluctuations in X and Y coordinates for translational errors are rather greater at the initial stage of simulation. As indicated earlier, spacecraft was driven by negative direction aerodynamic force suddenly at $t \geq 0$ s, even though control force was acting on the system with delay of 0.1 s. This reaction at initial stage induces corresponding changes in velocity and in acceleration which induce helium II slosh dynamics and produce fluid reaction forces and torques fed back to the spacecraft system. These large amplitude slosh oscillations gradually damp out and the system becomes low amplitude oscillations after $t > 200$ s. Under the control system described, translational acceleration, velocity and displacement errors are relatively small and below the range of the effectiveness of control.

Absolute values of maximum spacecraft translational accelerations deviating from normal operation are $(|a_x|, |a_y|, |a_z|) = (1.03, 2.03, 0.78)10^{-4}$ cm/s^2, while the range of maximum fluctuations of spacecraft acceleration deviating from normal operation are $(\Delta a_x, \Delta a_y, \Delta a_z) = (1.69, 3.70, 1.43)10^{-4}$ cm/s^2. Absolute values of maximum spacecraft translational velocities deviating from normal operation are $(|V_x|, |V_y|, |V_z|) = (11.71, 2.84, 2.05)10^{-3}$ cm/s, while the range of maximum fluctuations of spacecraft velocities deviating from normal operation are $(\Delta V_x, \Delta V_y, \Delta V_z) = (2.63, 5.61, 3.52)10^{-5}$ cm/s. Absolute values of maximum spacecraft translational displacement deviating from normal operation are $(|X|, |Y|, |Z|) = (1.03, 2.03, 0.78)10^{-3}$ cm, while the range of maximum fluctuations of spacecraft displacement deviating from normal operation are $(\Delta X, \Delta Y, \Delta Z) =$

24

$(1.69, 3.70, 1.43)10^{-5}$ cm.

As indicated earlier, computed results of translational acceleration, velocity and displacement will be amplified if sensor sensitivity and/or measurement errors are estimated and taken into consideration.

XI Conclusions and Discussion

It is shown in this simulation that the value of maximum variations of spacecraft attitude are on the order of 10^{-6} rad while spacecraft translational errors are on the order of 10^{-5} cm, with the activation of control system under normal operation. The level of spacecraft accelerations are on the order of 10^{-4} cm/s^2 which is also equivalent to 10^{-7} g$_0$ (g$_0$ = 9.81 m/s^2). In this simulation, with the neglection of initial stage and considering only for t>200 s, the level of spacecraft acceleration will be reduced to 10^{-6} cm/s^2 which is also equivalent to 10^{-9} g$_0$.

In this simulation, it is shown that control forces and torques required to carry over the necessary control processes are below the projected saturation values of the design requirements.

The simulated values of spacecraft angular rate errors and spacecraft attitude errors will be amplified if sensor sensitivity and measurement errors are estimated and are included in the model computation.

In this simulation, it is assumed that the fluid system was suddenly driven by environmental disturbances which cause relatively severe fluctuations of environmental forces and torques. This also implies that any large amplitude fluctuations can introduce large slosh dynamics which may cause a large disturbances which will be. deviating spacecraft from normal operation.

In this simulation, it is shown that under the considered environmental disturbances, the spacecraft is under the safe side to be considered within the accuracy of spacecraft control system.

Acknowledgement

References

1. Avduyevsky, V. S. (editor), <u>Scientific Foundations of Space Manufactureing</u>, MIR, Moscow, USSR, 1984, pp. 450.

2. Forward, R. L., "Flattening Space-Time Near the Earth," <u>Physical Review</u>, <u>Series</u> (A), Vol. 26, No. 5, 1982, pp. 735-744.

3. Misner, C. W., Thorne, K. S., and Wheeler, J. A., <u>Gravitation</u>, W. H. Freeman and Co., San Francisco, CA, 1973, pp. 253-674.

4. Kamotani, Y., Prasad, A., and Ostrach, S., "Thermal Convection in an Enclosure Due to Vibrations Aboard a Spacecraft," <u>AIAA Journal</u>, Vol. 19, No. 4, 1981, pp. 511-516.

5. Hung, R. J., Lee, C. C., and Leslie, F. W., "Spacecraft Dynamical Distribution of Fluid Stresses Activated by Gravity Jitters Induced Slosh Waves," <u>Journal of Guidance, Control and Dynamics</u>, Vol. 15, No. 3, 1992, pp. 817-824.

6. Hung, R.J., Lee, C.C., and Leslie, F.W., "Similarity Rules in Gravity Jitter-Related Spacecraft Liquid Propellant Slosh Waves Excitation," <u>Journal of Fluids and Structures</u>, Vol.<u>6</u>, No.3, 1992, pp. 493-522.

7. Hung, R.J., Tao, Y.D., Hong, B.B., and Leslie, F.W., "Bubble Behaviors in a Slowly Rotating Helium Dewar in Gravity Probe-B Spacecraft Experiment," <u>Journal of Spacecraft and Rockets</u>, Vol.<u>26</u>, N.1 1989, pp, 167-172.

8. Leslie, F. W., "Measurements of Rotating Bubble Shapes in a Low Gravity Environment," <u>Journal of Fluid Mechanics</u>, Vol. 161, No. 2, 1985, pp. 269-279.

9. Mason, P., Collins, D., Petrac, D., Yang, L., Edeskuty, F., Schuch, A., and Williamson, K., "The Behavior of Superfluid Helium in Zero Gravity," <u>Proc. 7th International Cryogenic Engineering Conferences</u>, Surrey, England, Science and Technology Press, 1978, pp. 101-114.

10. Donnelly, R.J., "Superfluid Turbulence", <u>Scientific American</u>, Nov. 1988, pp. 100-112.

11. Van Sciver, S. W., <u>Helium Cryogenics</u>, Plenium, New York, 1986, pp. 429.

12. Donnelly, R. J., <u>Quantized Vortices in Helium II</u>, Cambridge University Press, Cambridge, 1991, pp. 384.

13. Wilks, J., and Betts, D.S., <u>An Introduction to Liquid Helium</u>, 2nd edition, Clarendon Press, Oxford, 1987, pp. 187.

14. Hung, R. J., Pan, H. L., and Long, Y. T., "Peculiar Behavior of Helium II Disturbances Due to Sloshing Dynamics Driven by Jitter Accelerations Associated with Slew Motion in Microgravity," Cryogenics, Vol. 34 No.8, 1994, pp. 641-648.

15. Hung, R.J., and Long, Y.T., "Effect of Baffle on Slosh Reaction Forces in Rotating Liquid Helium Subjected to a Lateral Impulse in Microgravity", Cryogenics, Vol. 35, 1995, pp. 589-597.

16. Wilks, J., The Properties of Liquid and Solid Helium, Clarendon Press, Oxford, UK, 1967.

17. Hoare, F.E., Jackson, L.C. and Kurti, N., Experimental Cryogenics: Liquid Helium II, Butterworths, London, UK, 1961.

18. Hung, R.J., and Long, Y.T., "Response and Decay of Rotating Cryogenic Liquid Reacted to Impulsive Accelerations in Microgravity", Transaction of Japan Society for Aeronautical and Space Sciences, Vol. 37, No.2, 1995, 291-310.

19. Hung, R.J., and Pan, H.L., "Fluid Force Activated Spacecraft Dynamics Driven by Gravity Gradient and Jitter Accelerations", Journal of Guidance, Control, and Dynamics, Vol.18, 1995, pp. 1190-1196.

20. Hung, R. J., and Pan, H. L., "Differences in Gravity Gradient and Gravity Jitter Excited Slosh Waves in Microgravity," Transaction of the Japan Society for Aeronautical and Space Sciences, Vol. 36, No. 1, 1993, pp. 153-169.

21. Hung, R. J., and Pan, H. L., "Gravity Gradient or Gravity Jitter Induced Viscous Stress and Moment Fluctuations in Microgravity," Fluid Dynamics Research, Vol. 34, No. 1, 1994, pp.29-44.

22. Hung, R.J., Pan, H.L., and Leslie, F.W., "Fluid System Angular Momentum and Moment Fluctuations Driven by Gravity Gradient and Gravity Jitter in Microgravity," Journal of Flight Sciences and Space Research, Vol.18, No.1, 1994, pp. 195-202.

23. Hung, R. J., and Pan, H. L., "Asymmetric Slosh Wave Excitation in Liquid-Vapor Interface Under Microgravity," Acta Mechanica Sinica, Vol. 9, No. 2, 1993, pp. 298-311.

24. Hung, R.J., and Pan, H.L., "Mathematical Model of Bubble Sloshing Dynamics for Cryogenic Liquid Helium in Orbital Spacecraft Dewar Container" Applied

Mathematical Modelling, Vol 19, No. 8, 1995, pp. 483-498.

25. Hung, R.J., and Leslie, F.W., "Bubble Shapes in a Liquid-Filled Rotating Container Under Low Gravity", Journal of Spacecraft and Rockets, Vol. 25, No. 1, 1988, pp. 70-74.

26. Harlow, F. H., and Welch, F. E., "Numerical Calculation of Time-Dependent Viscous Incompressible Flow of Fluid with Free Surface," Physics of Fluids, Vol. 8, No. 11, 1965, pp. 2182-2189.

27. Rubin, S. G., and Lin, T. C., "A Numerical Method for Three-Dimensional Viscous Flow: Application to the Hypersonic Leading Edge," Journal of Computational Physics, Vol. 9, No. 3, 1972, pp. 339-364.

28. Salvadori, M. G., and Baron, M. L., Numerical Method in Engineering, Prentice-Hall, Inc., Englewood Cliffs, NJ, 1961, pp. 37-252.

29. Hageman, L. A., and Young, D. M., Applied Iterative Methods, Academic Press, New York, 1981, pp. 21-168.

30. Young, D., "Iterative Methods for Solving Partial Difference Equations of Elliptical Type," Transactions of American Mathematical Society, Vol. 76, No. 2, 1954, pp. 92-111.

31. Patanker, S. V., "Numerical Heat Transfer and Fluid Flow", Hemisphere-McGraw-Hill, New York, NY, 1980, pp. 197.

32. Dougherty, H. J., Relatively Mission-Gravity Probe-B "System Design and Documentation-Force and Torque Model", LMSC/P086702, Locheed-Martin, 28 Sunnyvale, CA, 1995, pp. 105.

33. Dougherty, H. J., Relativity Mission-Gravity Probe-B " System Design and Documentation-Attitude and Translational Control Subsystem Description", LMSC/P086701, Lockheed-Martin, Sunnyvale, CA, 1995, pp. 57.

34. Greenwood, D.T., Principles of Dynamics, Prentice- Hall, Englewood Cliffs, N.J., 1965, pp. 518.

35. Hung, R. J., Lee, C. C., and Leslie, F. W., "Effect of the Baffle on the Spacecraft Fluid Propellant Viscous Stress and Moment Fluctuations "Transactions of the Japan Society for Aeronautical and Space Sciences, Vol. 35, No. 2, 1993, pp. 187-207.

36. Hung, R. J., and Lee, C. C., "Effect of a Baffle on Slosh Waves Excited by Gravity Gradient Acceleration in Microgravity," Journal of Spacecraft and Rockets, Vol. 31, No.6, 1994, pp. 1107-1114.

Figure Captions

Figure 1   Computational algorithm for sloshing dynamics.

Figure 2   (A) Geometry of gravity gradient acceleration, (B) Time evolution of aerodynamic forces.

Figure 3   Time evolution of environmental disturbance torques acting on spacecraft during a full orbital period. (A) Gravity gradient torques, (B) Aerodynamic torques, and (C) Magnetic torques.

Figure 4   Computational algorithm for solving slosh dynamics of fluid equations in conjunction with translational and rotational equations of orbital dynamics and in coupling with translation and attitude control equations to carry out control processes.

Figure 5   (A) Grid generation, (A-a) three-dimensional dewar, (A-b) r-z plane at $\theta=0°$, (A-c) r-θ plane at z=L/2 (L=height of dewar); (B) Initial profile of liquid-vapor interface, (B-a) three-dimensional interface, (B-b) r-z plane at $\theta=0°$, (B-c) r-θ plane at z=108 cm.

Figure 6   Time sequence evolution of three-dimensional liquid-vapor interface driven by combined environmental disturnbanes including gravity gradient forces and torques, aerodynamic forces and torques, and magnetic torques, coupling with spacecraft dynamics.

Figure 7   Time evolution of fluid mass center fluctuations along (x,y,z) directions (in rotational frame) acting on dewar driven by the combination of gravity gradient forces and torques, aerodynamic forces and torques, and magnetic torques.

Figure 8   (A) Time evolution of slosh reaction forces (in rotational frame) along (x,y,z) directions driven by combined gravity gradient forces and torques, aerodynamic forces and torques, and magnetic torques. (B) Time evolution of slosh reaction torques (in rotational frame) acting on dewar driven by the similar combined environmental forces and torques.
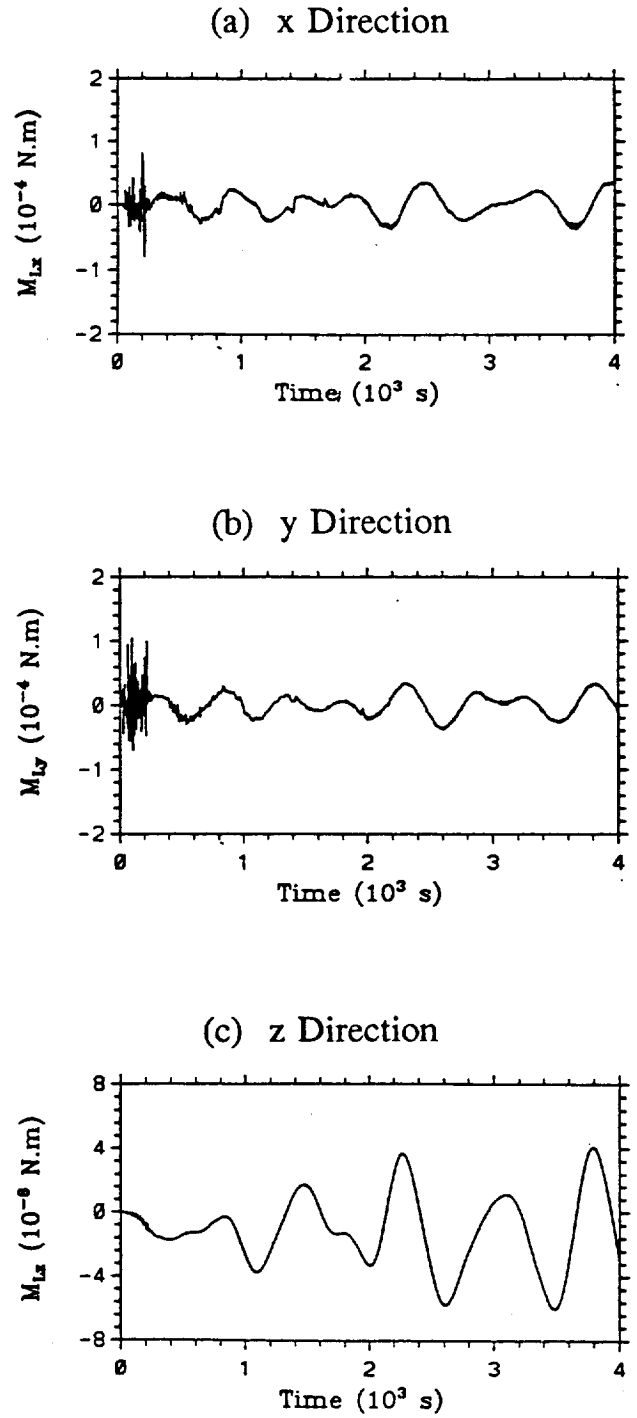
Figure 9   Power spectral density of slosh reaction forces and torques acting

including gravity gradient forces and torques, aerodynamic forces and torques, and magnetic torques. (A) Slosh reaction forces, and (B) Slosh reaction torques.

Figure 10   Time evolution of control forces (in non-rotational frame) acting on spacecraft based on the translation and attitude control equations. (A) Components of control forces, and (B) Conponents of control torques.

Figure 11   Time evolution of total resultant forces and torques acting on the spacecraft with the activation of control system under normal operation. (A) Total resultant forces and (B) Total resultant torques.

Figure 12   Time evolution of spacecraft angular rate errors and attitude errors (in rotating frame) with the activation of control system under normal operation. (A) Spacecraft angular rate errors and (B) Spacecraft attitude errors.

Figure 13   Time evolution of translational acceleration, velocity and displacement errors with the activation of control system under normal operation. (A) Translational acceleration errors, (B) Translational velocity errors and (C) Translational displacement errors.

Computational Algorithm for Sloshing Dynamics
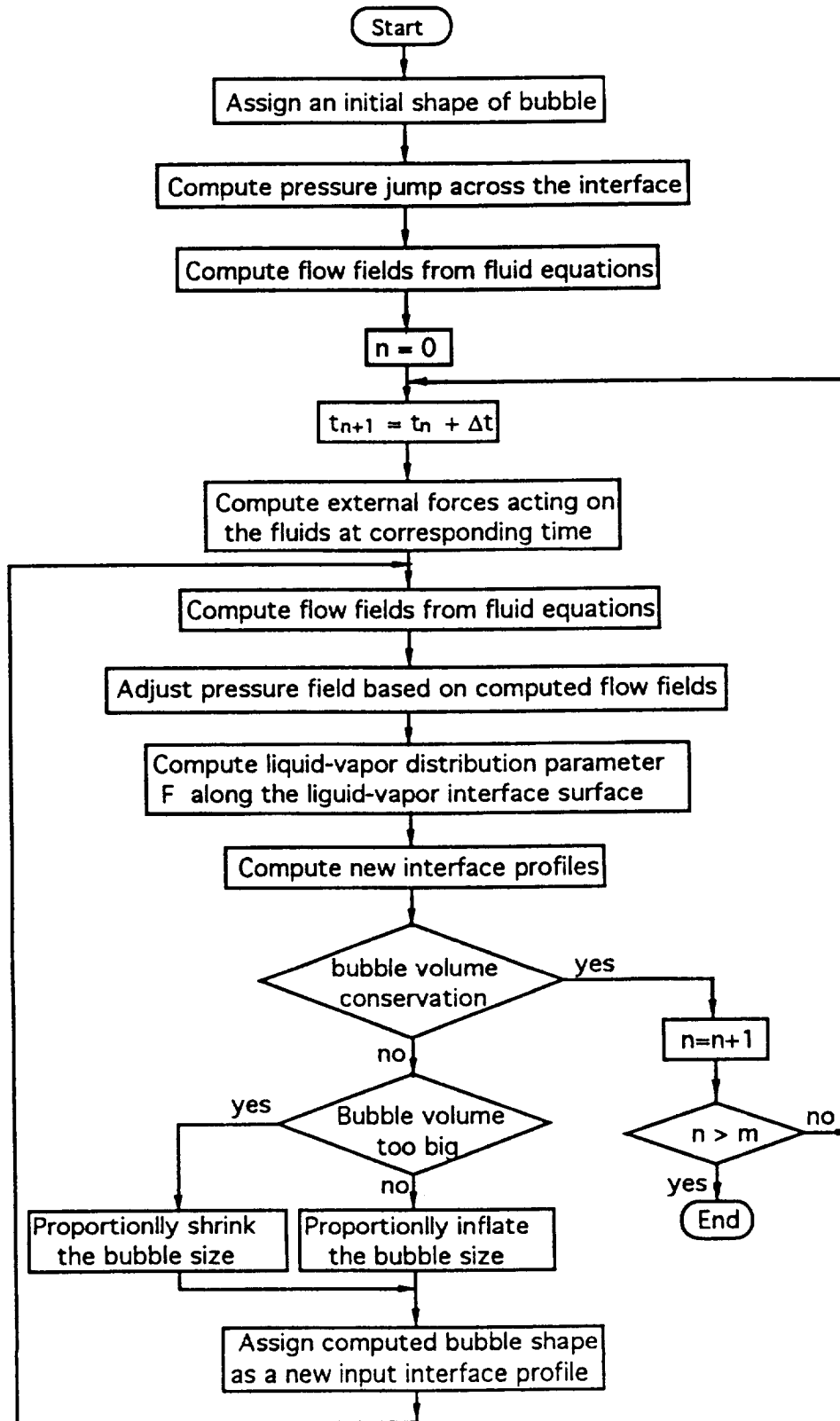
Fig. 1

(A) Geometry of Gravity Gradient Acceleration
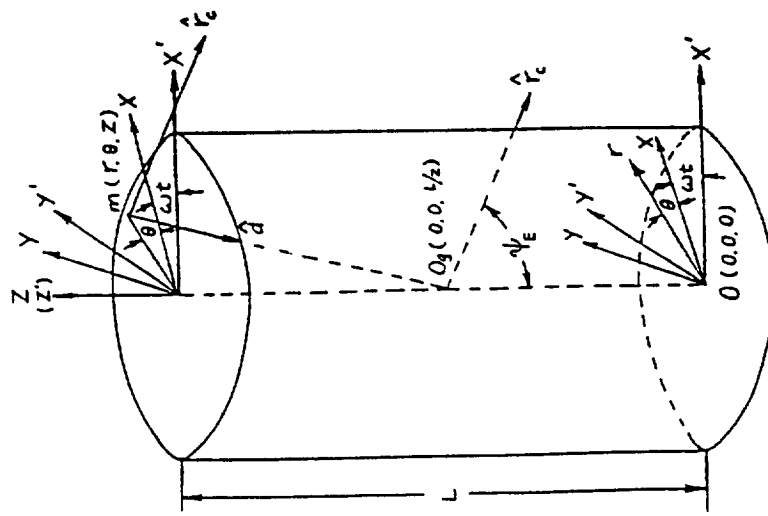
(B) Time Evolution of Aerodynamic
Force Disturbances
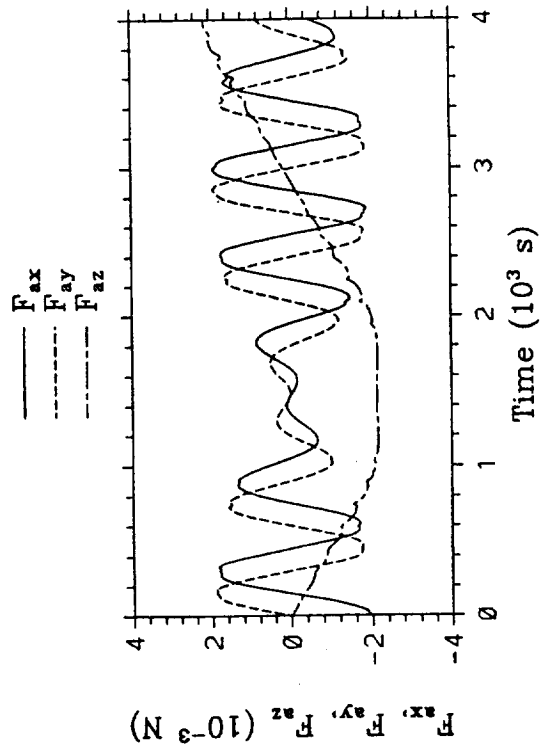
Fig. 2

ENVIROMENTAL DISTURBANCE TORQUES

(A) Gravity Gradient Torques

(B) Aerodynamic Torques

(C) Magnetic Torques

Fig. 3

Computational Algorithm for Solving Slosh Dynamics of Fluid Equations in Conjunction with Translational and Rotational Equations of Orbital Dynamics and in Coupling with Translation and Attitude Control Equations to Carry out Control Processes

$$\text{Start}$$

$$t = 0, \Delta t = 0.1 \text{ s}, \ t_{max} = 4000 \text{ s}$$

Initialization (at t = 0) :

$$X_i = 0, \ \dot{X}_i = 0, \ \ddot{X}_i = 0, \ \dot{\theta}_1 = \dot{\theta}_2 = 0, \ \dot{\theta}_3 = \omega, \ \ddot{\theta}_i = 0, \ F_{Li} = 0, \ M_{Li} = 0, \ F_{Ci} = 0, \ M_{Ci} = 0,$$

Orbital Forces & Torques: F_{ai} , M_{ai} , F_{mi} , M_{mi} , F_{gi} , M_{gi}

Resultant Force & Torque: $F_{Si} = F_{ai} + F_{mi} + F_{gi} + F_{Li} + F_{Ci}$,

$$M_{Si} = M_{ai} + M_{mi} + M_{gi} + M_{Li} + M_{Ci}$$

$$t = t + \Delta t$$

Solve Translational Eq. to obtain X_i , $\dot{X}_i$ & $\ddot{X}_i$ in Non - Rotational Frame

Solve Rotational Eq. to obtain θ_i , $\dot{\theta}_i$ & $\ddot{\theta}_i$ in Rotational Frame

Put $\ddot{X}_i$, $\dot{\theta}_i$ & $\ddot{\theta}_i$ in Flui Eq. and solve it to obtain F_{Li} & M_{Li}

Calculate Orbital Forces & Torques: F_{ai} , M_{ai} , F_{mi} , M_{mi} , F_{gi} , M_{gi}

$$|\theta_i| < \varepsilon_\theta \ \& \ |X_i| < \varepsilon_X$$

Put X_i in Translational Control Eq. to calculate F_{Ci}

Put θ_i & $\dot{\theta}_i$ in Attitude Control Eq. to calculate M_{Ci}

$$F_{Ci} = 0, \ M_{Ci} = 0$$

Calculate Resultant Force & Torque:
$$F_{Si} = F_{ai} + F_{mi} + F_{gi} + F_{Li} + F_{Ci}$$
$$M_{Si} = M_{ai} + M_{mi} + M_{gi} + M_{Li} + M_{Ci}$$

$$t > t_{max}$$

Output

Stop

Fig. 4

(A) Grid Generation

(a) 3-D

(b) r - z plane

(c) r - θ plane

(B) Initial Profiles

(a) 3-D

(b) r - z plane

(c) r - θ plane

Fig. 5

Time Sequence Evolution of Three-dimensional Liquid-vapor Interface

(A) t = 0 s
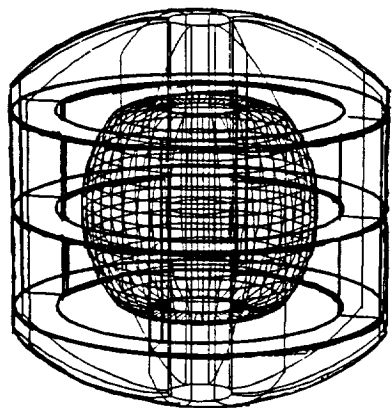
(B) t = 800 s
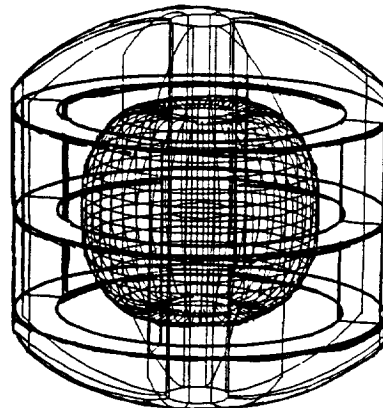
(C) t = 1600 s
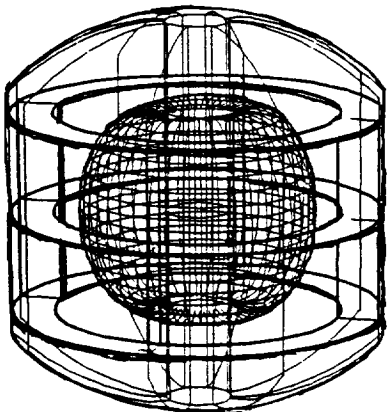
(D) t = 2400 s
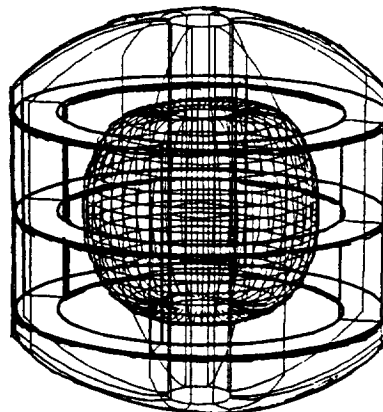
(E) t = 3200 s
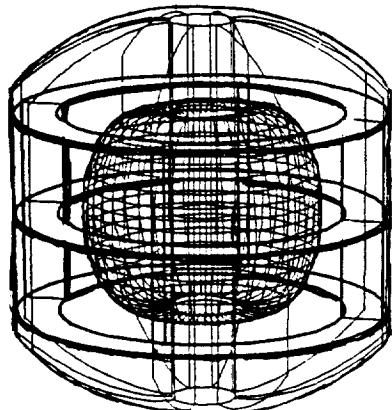
(F) t = 4000 s
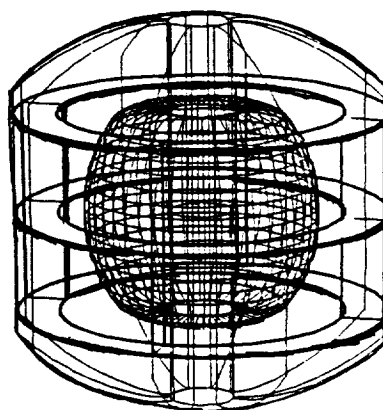
Fig. 6

Time Evolution of Fluid Mass Center Fluctuations
(in rotational frame)

(A) x Direction
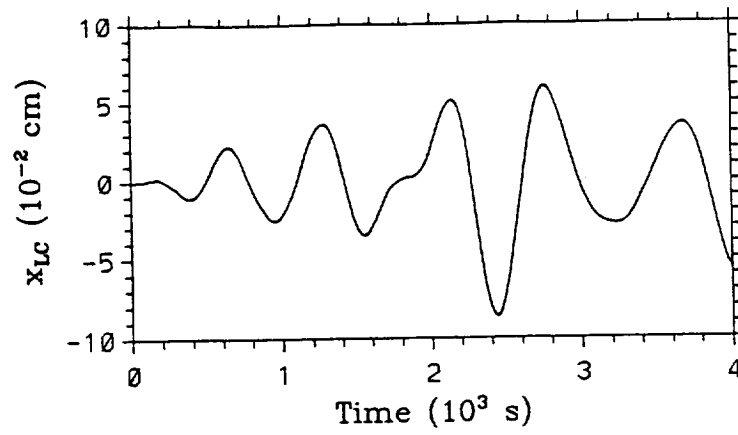
(B) y Direction
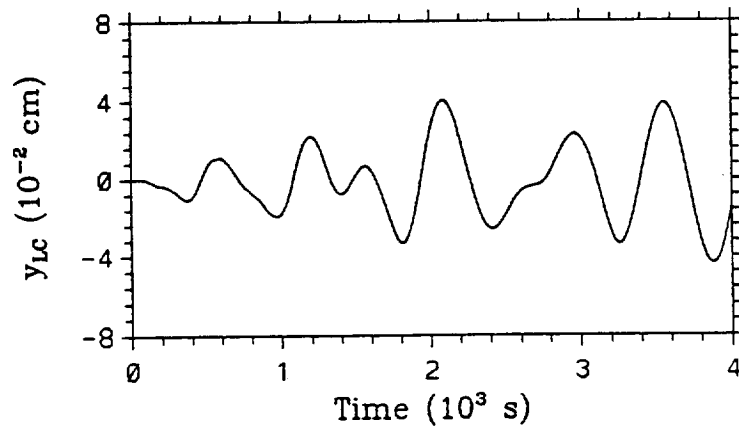
(C) z Direction
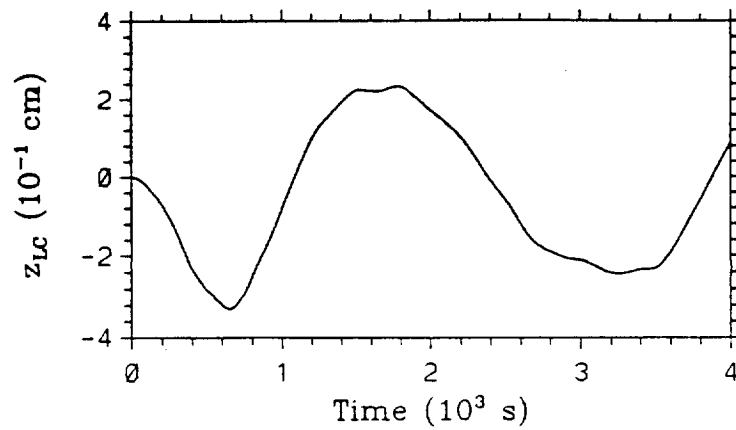
Fig. 7

Time Evolution of Slosh Reaction Forces (in rotational frame) Driven by
Environmental Forces and Torques Coupling with Spacecraft Dynamics

(A) Slosh Reaction Forces

(B) Slosh Reaction Torques

(a) x Direction

(a) x Direction

(b) y Direction

(b) y Direction

(c) z Direction
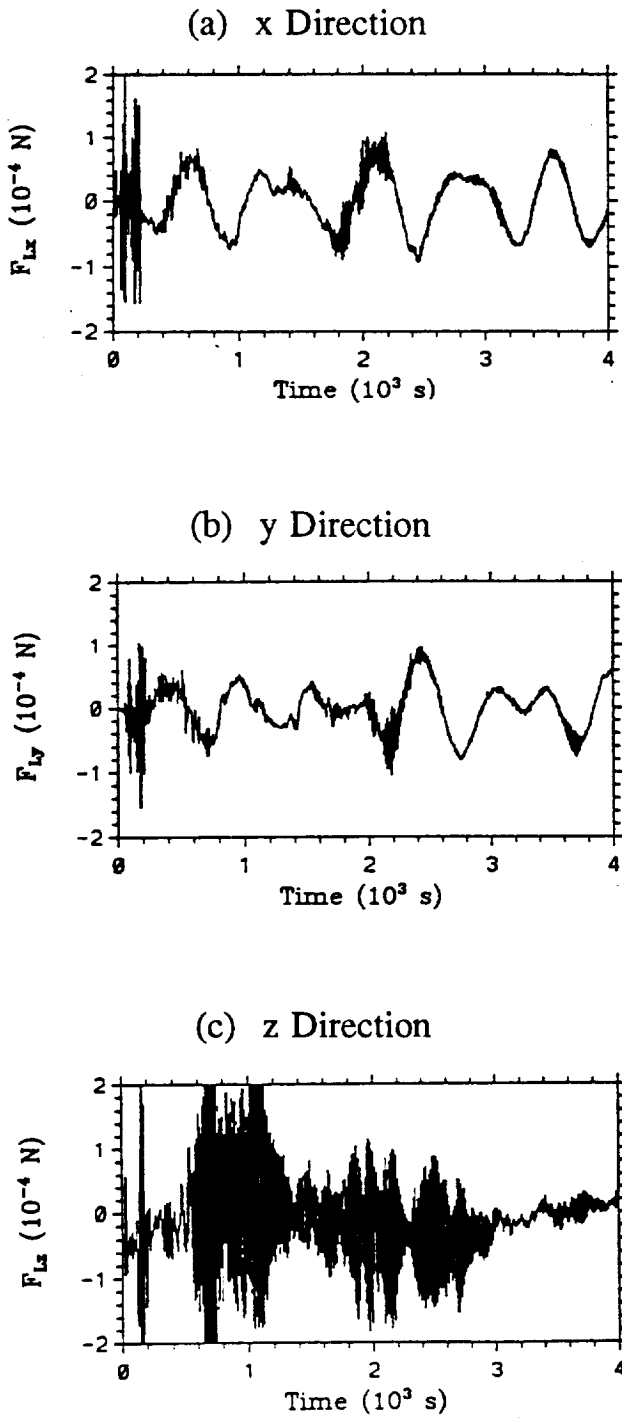
(c) z Direction

Fig. 8

Power Spectral Density of Slosh Reaction Forces and Torques Acting on the Dewar
Driven by Environmental Forces and Torques Coupling with Spacecraft Dynamics

(A) Slosh Reaction Forces

(B) Slosh Reaction Torques

(a) x Direction
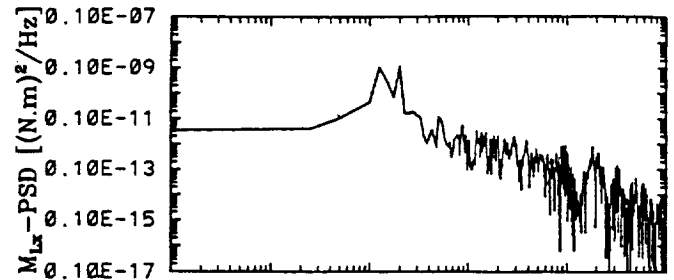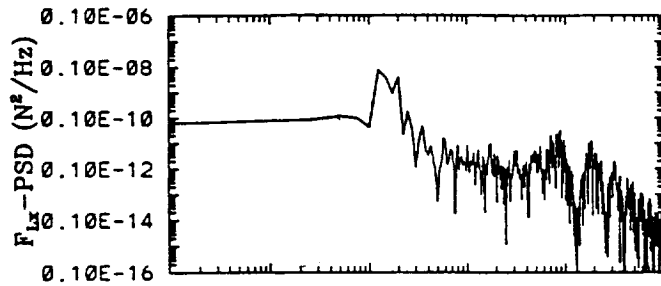
(a) x Direction

(b) y Direction
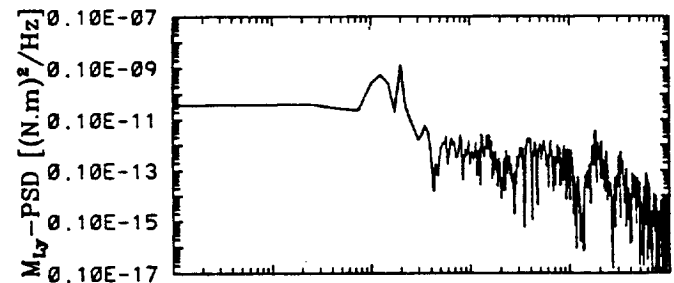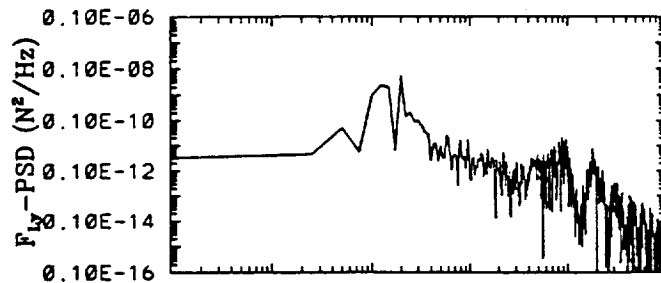
(b) y Direction

(c) z Direction
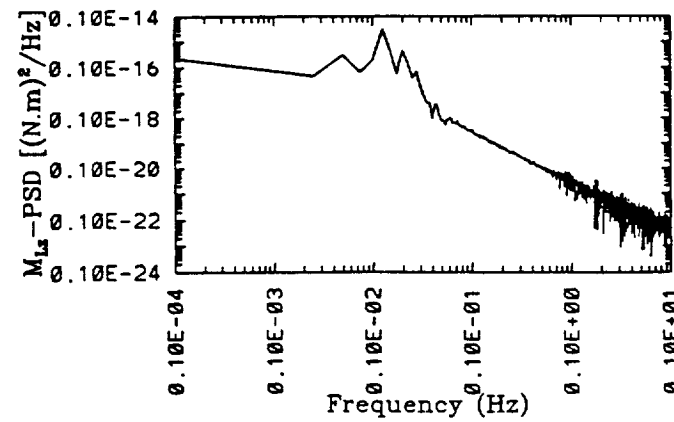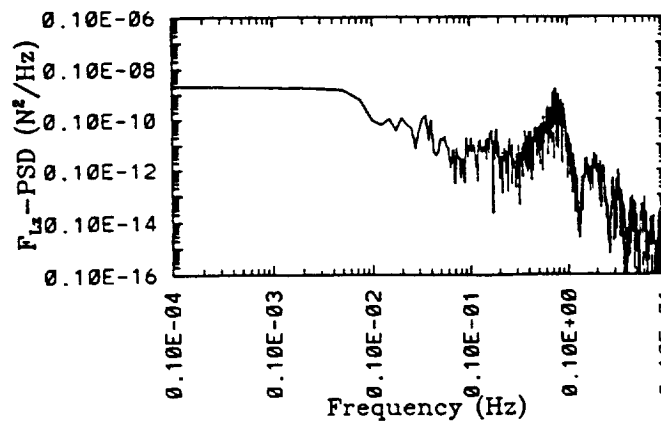
(c) z Direction

Fig. 9

Time Evolution of Control Forces and Torques Acting on Spacecraft Based on the Translation and Attitude Control Equations

(A) Control Forces
(a) x Direction
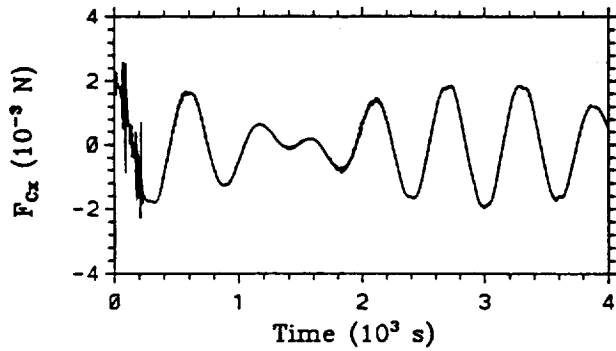
(B) Control Torques.
(a) x Direction
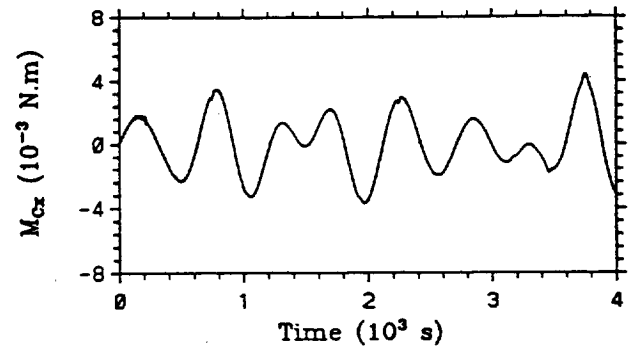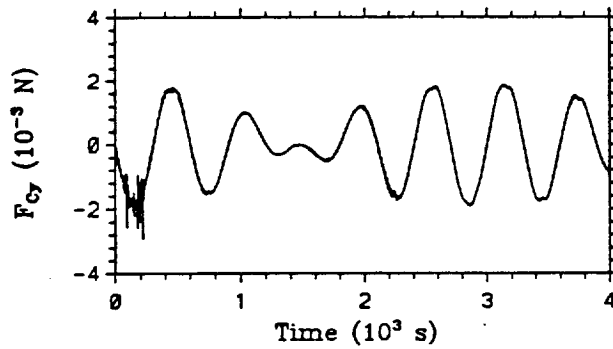
(b) y Direction
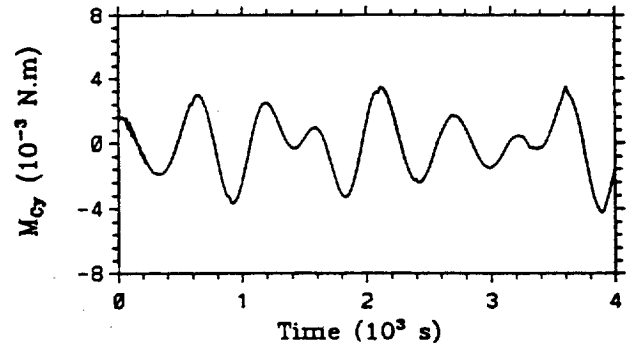
(b) y Direction
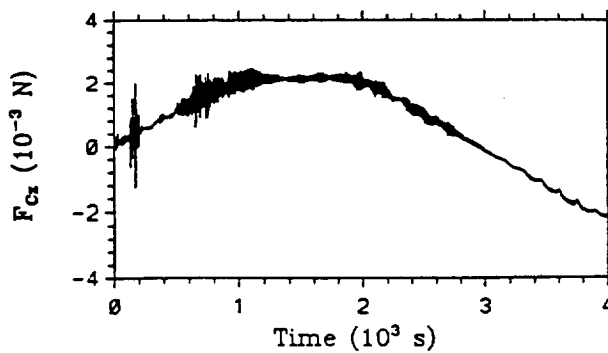
(c) z Direction
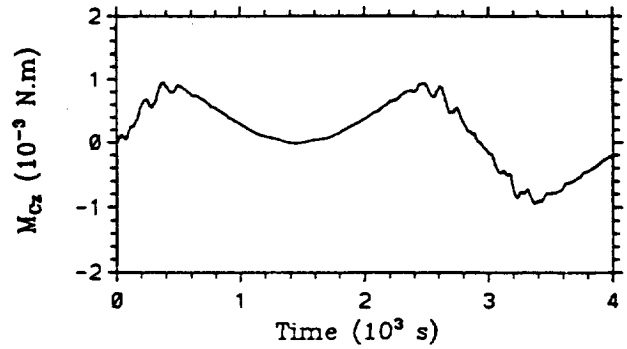
(c) z Direction

Fig. 10

Time Evolution of Total Resultant Forces and Torques Acting on Spacecraft with Activation of Control System under Normal Operation

(A) Total Resultant Forces

(a) x Direction

(b) y Direction

(c) z Direction

(B) Total Resultant Torques.

(a) x Direction
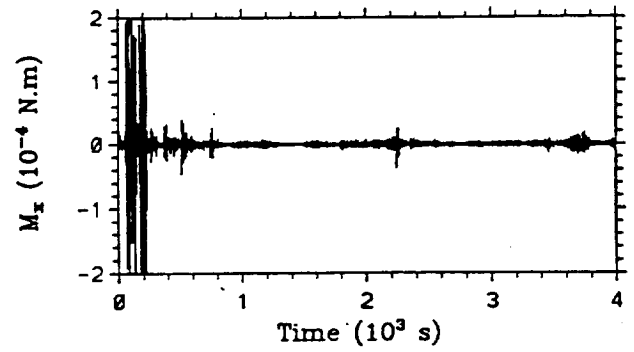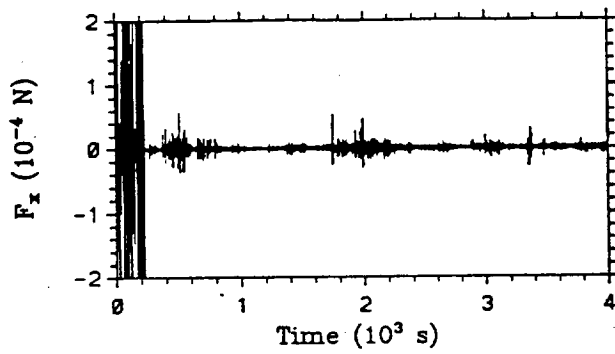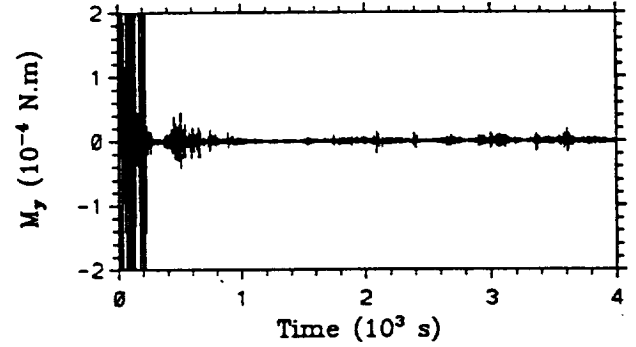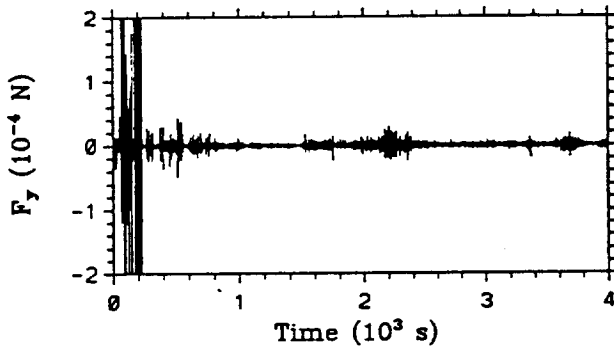
(b) y Direction

(c) z Direction
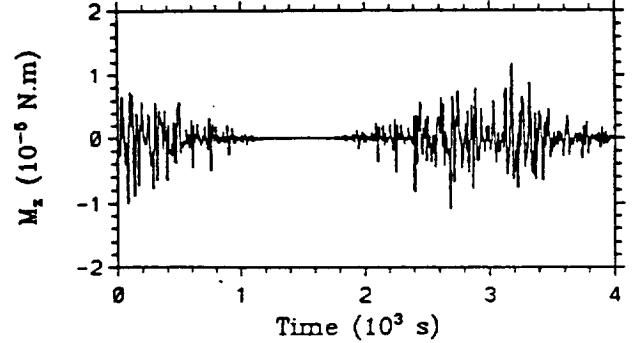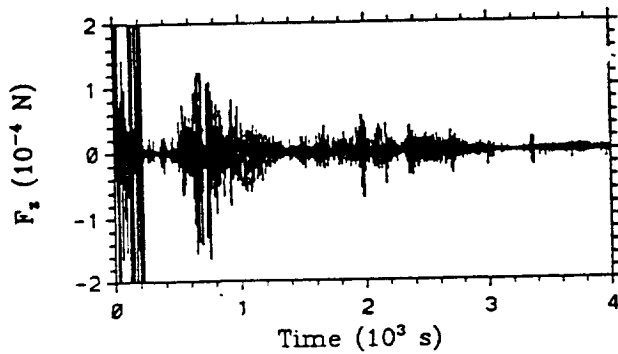
Fig. 11

Time Evolution of Spacecraft Angular Rate Errors and Attitude Errors (in Rotating Frame) with Activation of Control System under Normal Operation

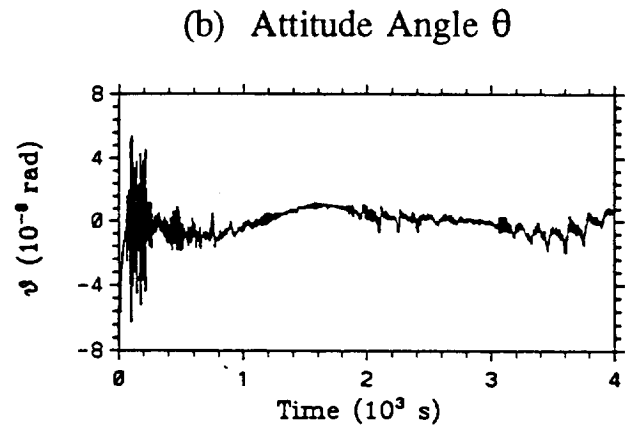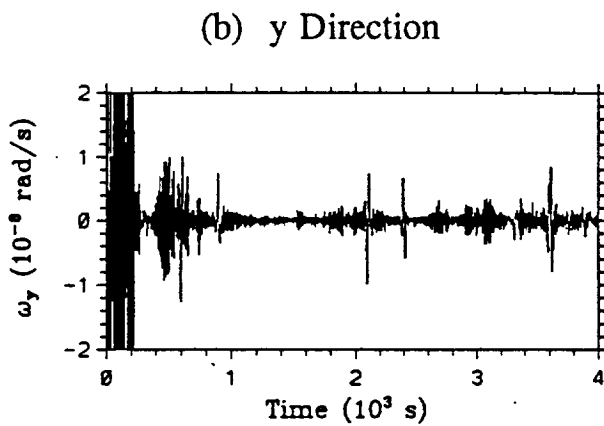(A) Spacecraft Angular Rate Errors   (B) Spacecraft Attitude Errors

(a) x Direction   (a) Heading Angle ψ

(b) y Direction   (b) Attitude Angle θ

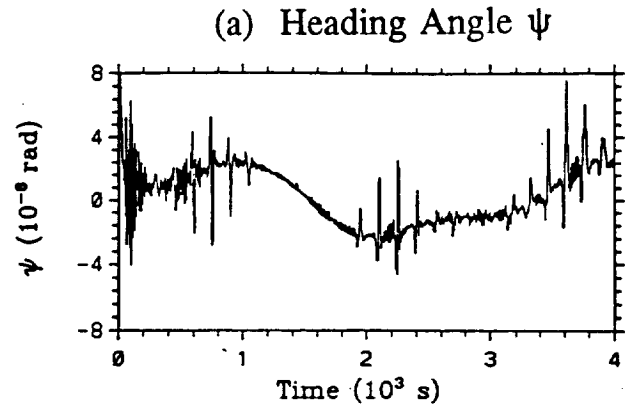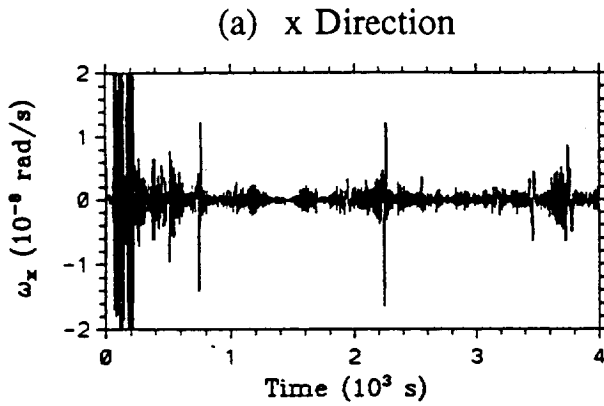(c) z Direction   (c) Bank Angle $\Delta\phi$
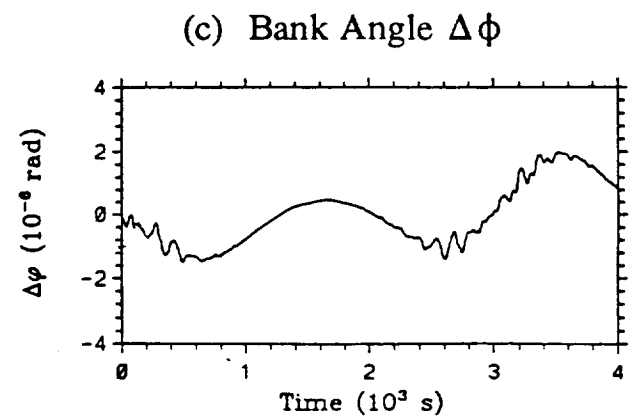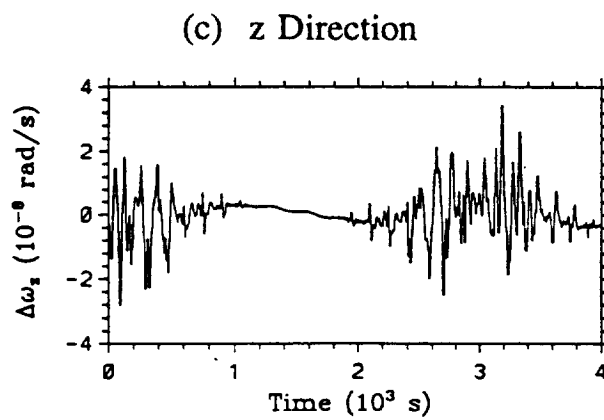
Fig. 12

Time evolution of Translational Acceleration, Velocity and Displacement Errors
with Activation of Control System under Normal Operation

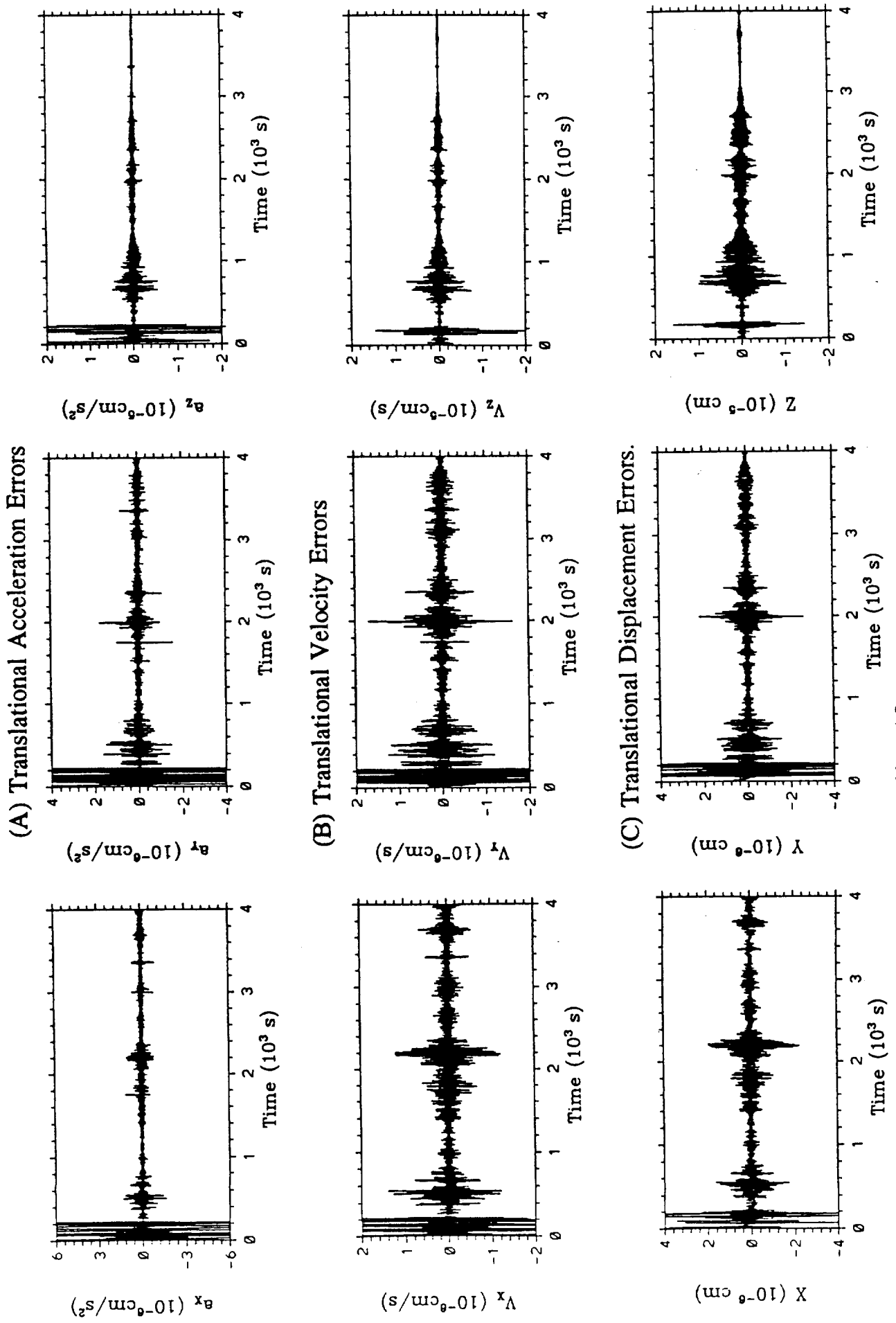(A) Translational Acceleration Errors

(B) Translational Velocity Errors

(C) Translational Displacement Errors.

Fig. 13